An Axisymmetric Model for the Charging and Discharging Cycle of a PCM-Enhanced Domestic Hot Water Tank

Dave van der Stoel

September 19, 2020

Preface

First of all I would like my supervisor Prof. dr. ir. B.J. Boersma for guiding me throughout this thesis and for providing me with a lot of useful information. Secondly, I would like to thank ir. W. de Vries from Inventum for guiding me through more practical problems I encountered.

Due to Covid-19, I switched from an experimental thesis to a model based thesis and I am thankful that both dr. ir. B.J. Boersma and ir. W. de Vries accepted this change.

Finally I would like to thank my family and friends for their indirect help to finish this report.

Abstract

In the report that is before you, a method has been investigated to increase the capacity of domestic hot water tanks. To do so without having to increase the volume of the tank, a phase change material has been included in an annular space around the tank. To test the performance of such a system, three main topics are dealt with in this report.

First of all, the most suitable phase change material was selected. There exist many types of phase change materials, all having completely different properties, advantages and disadvantages.

Secondly, weak spots were indicated during melting of the phase change material. These spots indicate the locations of the worst heat transfer rate, and to improve the performance of the system, these spots can be treated separately in future experiments or models, for example by placing fins at those locations.

Finally, the response time of the phase change material was investigated during a typical discharge cycle to investigate the amount of latent heat that was released to the water.

To model the charging- and discharging cycle, the vorticity stream method was used to create a two dimensional axisymmetric model. This model was implemented into MATLAB. The Boussinesque approximation was assumed to take into account buoyancy effects. Furthermore, only diffusive heat transfer was assumed to take place throughout the PCM and the effect of convection was neglected.

Results showed that paraffin based PCMs are most suitable for applications in domestic hot water tanks. They are inert and stable, and their thermal properties do not degrade in time. They have suitable melting temperatures and high latent heat. To increase the thermal conductivity, dispersion of high density alumina particles was applied.

Although the charging model did not reach the asymptotic range of convergence, it was shown that melting 5.0 cm PCM required long periods of time. After 9 hours, part of the PCM was still in its solid phase. Due to thermal stratification in the tank, the slowest melting rate was seen at the lower outer edges of the tank.

During the discharge cycle, it was shown that not all PCM was able to release its latent heat to the water: 16.9% did not solidify. This occurred at an adapted flow rate to match the discharge time for both tanks. For higher flow rates, used in domestic hot water tanks, the amount of liquid PCM would even be greater, resulting in less latent energy release to the water.

Based on the fact that 5.0 cm PCM did not increase the heat capacity of the tank, and all the previously mentioned factors, it is concluded that the performance of a hot water tank enhanced with PCM in an annular space does not increase the performance of a domestic hot water tank. Some suggestions were made regarding the possibilities of increasing the performance of the tank in future models and experiments.

Nomenclature

Symbol	Meaning
A	Sorbent
ARC	Asymptotic range of convergence
B	Sorbate
c (or c_p)	Specific heat capacity [J/(kgK)] (at constant pressure)
e	Volume fraction of dispersed particles over PCM-volume
err	Error
Fo_r	Radial Fourier number ($\alpha_s \Delta t/\Delta r^2$)
Fo_z	Axial Fourier number ($\alpha_s \Delta t/\Delta z^2$)
F_s	Safety factor (1.25)
g	Acceleration of gravity [m/s^2]
Gr	Grashof number ($g\beta(T_h - T_o)h^3/\nu^2$)
GCI	Grid convergence index
H	Specific enthalpy PCM [J/kg]
HWT	Hot water tank
h	Tank height [m]
k	Thermal conductivity [W/(mK)]
L	Latent heat [J/kg]
m	Mass [kg]
n_pcm	Number of radial nodes in PCM region
n_r	Number of radial nodes in water region
n_z	Number of axial nodes
p	Order of convergence
PCM(s)	Phase change material(s)
Pe	Peclet number ($u_\mathrm{jet}h/\alpha$)
Pr	Prandtl number (ν/α)
Q	Heat [J]
q	Volumetric heat generation [W/m^3]
Q_v	Volumetric inflow [m^3/s]
r	Dimensionless radial distance from the axis of symmetry
Re	Reynolds number ($u_\mathrm{jet}h/\nu$)
Ri	Richardson number ($g\beta(T_o - T_h)h/u_\mathrm{jet}^2$)
r_i	Dimensionless location of interface
r_o	Dimensionless outer radius of the tank
T	Temperature [°C]
t	Dimensionless time
u	Dimensionless axial velocity
v	Dimensionless radial velocity
V	Volume [m^3]
z	Dimensionless axial coordinate

Greek Symbol	Meaning
α	Thermal diffusivity [m^2/s]
β	Thermal expansion coefficient [K^{-1}]
ϵ	Controlling parameter for heater
λ	Conversion factor for PCM equations ($k_s/(\rho_s\alpha_s)$)
ν	Kinematic viscosity [m^2/s]
ρ	Density [kg/m^3]
σ	Dimensionless form for internal heat generation ($qh^2/(k(T_h - T_o))$
ϕ	Azimuthal component
Ψ	Dimensionless stream function
ω	Acceleration parameter for SOR-accelerated iteration
Ω	Dimensionless vorticity
Ω'	Modified vorticity (Ω/r)

Sub/Superscript	Meaning
coarse	Properties evaluated at coarse grid
cr	Critical
f	Final (state)
fine	Properties evaluated at fine grid
g	Gaseous (state)
h	Hot (maximum allowable temperature is T_h)
i	Axial nodal position
j	Radial nodal position
j^*	Modified Radial nodal position: $j^* = j + n_r$
jet	Property inside jet region
l	Liquid (state)
LHS	Latent heat storage
m	Melting
medium	Properties evaluated at medium grid
mix	Mixture of dispersed particle and PCM
o	Initial (state)
p	Particle
PCM	Phase change material
s (subscript)	Solid state (or PCM in case of modeling)
s (superscript)	Iteration number for SOR-accelerated iteration
SHS	Sensible heat storage
THS	Thermo-chemical heat storage
true	True properties based on order of convergence
w	Water
$*$	Normal property instead of dimensionless property

Contents

1 Introduction

The worldwide population is growing and so does the energy demand. The global energy demand is growing exponentially [29]. Fossil fuels such as coals, oil and gas are main contributors to the generation of energy, but it comes at a price. The worldwide pollution is increasing [29]. This results in a negative impact on the climate worldwide. Furthermore, fossil fuels are being depleted and the rate of using biomass or trees is exceeding the rate of these sources growing back [1]. For these reasons, energy efficiency has become a major objective for energy policy at regional, national and international levels [30].

In the residential sector, 16% of the total energy consumption is used for heating water. Nowadays, with well insulated new buildings, this percentage increased to 25% [1]. Space- and water heating combined almost cover 60% of the total energy consumption in the residential sector [1]. Compared with other sectors, 15% to 60% of the total energy consumption is consumed by the residential sector and averages up to 30% worldwide [28].

Because the degree of insulation on residential buildings is improving, relatively more energy is consumed by water heating. It would be an interesting objective to find methods to increase the overall performance of water heating applications. This thesis paper is aiming to do so by investigating methods to increase the energy capacity of domestic hot water tanks.

Hot water from tanks should be available at a minimum of 45.0 °C throughout the day to provide comfort to the user. However, to kill legionella bacteria, the water must be heated periodically to temperatures of around 60.0 °C [1]. To maintain these temperatures inside a hot water tank, heat must be added to the water to compensate for the ambient losses. To extend the availability of hot water in the tank, several solutions exist. Firstly, water saving taps and shower heads can be used. They reduce the amount of hot water usage and they are able to save up to 60% of the energy consumption for heating water [1]. Secondly, one can add more isolating material around the tank to reduce the ambient losses. Thirdly, the energy capacity of the tank can be increased. To increase the capacity, more water mass could be added to increase the thermal mass and delay the cooling process. However, the tank volume must be increased in order to do so. For small domestic hot water tanks, this would be impractical. Another option to increase the energy capacity is to use an external medium that is able to store and release heat to the water, when required. Unlike the previous solution, the volume of the tank remains unchanged. The external medium should be capable of storing and releasing a great amount of heat per unit volume.

This report will investigate the latter of these methods: using an external storage medium to increase the capacity of a hot water tank, without having to increase the tank volume. Three different methods exist to store heat inside an external medium: sensible heat storage, latent heat storage and thermo-chemical heat storage. These three methods will be investigated in chapter 2 and the most suitable method will be selected.

To test the benefits of the selected system, three goals are set for the remainder of the paper. First, the optimal material will be selected to use as an external medium. Secondly, the behaviour of this material is investigated during the phase change, which is necessary to store heat, and any weak spots will be outlined. Finally, the response time of the storage material will be investigated during the discharge cycle.

The tank of interest will be a domestic electrical hot water tank, used in the residential sector. Heat is added to the water by means of an electrical resistor located at the bottom of the tank. The storage medium will be a latent heat based storage medium: a paraffin based compound, RT 60 Rubitherm. Two modes of operation will be simulated: charging and discharging of the tank. A comparison will be made between a conventional hot water tank and a hot water tank with addition of a latent heat based storage medium. Both tanks will have equal volume. The comparison will be based on the energy input of both systems, and the outlet temperature during the discharge cycle. To simulate both processes, the streamfunction-vorticity method ($\psi - \Omega$) with an additional equation for the temperature has been implemented in MATLAB.

In the next chapter, more information will be provided regarding the three methods to store heat. The motivation for using a latent heat based storage medium will be presented. In chapter 3, information will be presented regarding the media that are capable of storing sensible heat, including the pros and cons. Furthermore, a selection of the most suitable material will be made and motivated in this chapter. In chapter 4, information will be presented regarding hot water tanks in general and their currently existing

models. In chapter 5 the models and assumptions will be presented. In chapter 6, the results are discussed. Chapter 7 will present conclusions and chapter 8 will present the recommendations for future models and experiments.

2 General Heat Storage

In this chapter, three methods of storing heat will be discussed: sensible heat, latent heat and thermo-chemical heat storage.

Sensible heat storage (SHS) is based on a temperature change of the storage material. The storage material can either be solids, liquids or even gases [2]. The amount of heat that can be stored depends on the mass of the storage material (m), the specific heat capacity of the storage material (c) and the magnitude of the temperature change. Often, the specific heat capacity is assumed to be constant over a small temperature change. Using this assumption, the amount of heat that can be stored is presented in equation 1:

$$Q_{\text{SHS}} = mc \int_{T_o}^{T_f} dT = mc(T_f - T_i) \tag{1}$$

In equation 1, the initial and final temperatures are denoted by T_o and T_f respectively. The same amount of energy, Q_{SHS}, is released when the temperature of the SHS medium decreases from T_f to T_o. Within the temperature range 0 - 100 °C, water is a popular sensible heat storage medium. It is cheap, non-toxic and has a high specific heat capacity compared to other materials. For higher temperatures, oils, molten salts and liquid metals are used [3]. For space heating applications, rocks are often used as heat storage medium [3]. Overall, sensible heat storage systems are simple, cheap and non-toxic. However, systems require large volumes of storage material in general.

Latent heat storage (LHS) is based on a phase change of the storage material. For pure substances, there is no temperature change during the phase change. Heat is stored or released at a constant temperature. This temperature is the melting/solidification temperature of the storage material. At phase change temperature, the amount of heat that is stored as latent heat is provided by equation 2.

$$Q_{\text{LHS}} = mL \tag{2}$$

In equation 2, the term L represents the latent heat of the storage material in J/kg. To illustrate the difference between sensible heat and latent heat, a simple example is given. Assume 1.0 kg of water needs to melt from its solid state to its liquid state. Since the phase is changed from solid to liquid, the latent heat is used to calculate the heat that was stored inside the ice, and is released when water is formed. In the case of water, 334 kJ is required to melt 1.0 kg of ice. The same is true for the opposite phase change: 334 kJ should be extracted to solidify 1.0 kg of water. The whole process takes place at the phase change temperature: 0 °C in the case of water. In terms of sensible heat, 334 kJ is equal to a temperature change of 80 °C for 1.0 kg water.

In most phase change applications, sensible heat and latent heat are both present. For example, if one wants to heat a block of ice from -10 °C to 10 °C. First, sensible heat is required to increase the temperature of the ice from -10 °C to its phase change temperature, 0 °C. Next, the phase change occurs when one keeps adding heat. When all latent heat has been added, all solid ice has turned into liquid water. Finally, sensible heat is required to heat the water from 0 °C to 10 °C. We could write this process mathematically as:

$$Q = mc_s \int_{T_o}^{T_m} dT + mL + mc_l \int_{T_m}^{T_f} dT = m(\mathrm{c}_s(T_m - T_o) + L + \mathrm{c}_l(T_f - T_m)) \tag{3}$$

In equation 3, T_o is the initial temperature, the phase change temperature has been represented by T_m and the final temperature is presented by T_f. In our previous example these temperatures are -10, 0 and 10 °C respectively. Note that specific heat capacity may change when the phase is changed from solid to liquid or vice versa. Therefore c_s and c_l are distinguished from one another: specific heat capacity for solids (s) and liquids (l) respectively. In figure 1 sensible heat storage (dashed line) is compared with latent heat storage (solid line). Assuming a constant specific heat capacity, a linear relation is found for the sensible heat storage regions. The first and last slope of figure 1 originate from the first and third term from equation 3 respectively. The isotherm originates from the second term in 3. In terms of our previous example: the

first slope represents heating ice from -10 °C to 0 °C and the second slope represents heating water from 0 °C to 10 °C. The constant temperature part represents the phase change itself, at 0 °C. The amount of heat stored inside the material increases when a phase change occurs, as can be seen from 1.

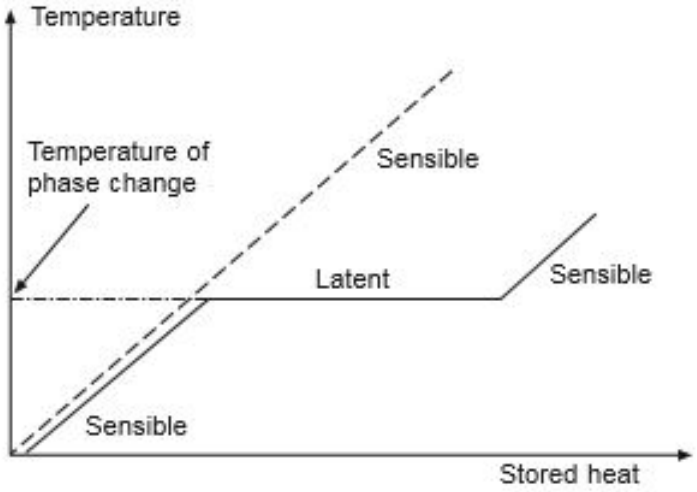

Figure 1: *Comparison between sensible heat storage (dashed line) and latent heat storage (solid line). Specific heat capacities are equal in the solid-and liquid phase. This may not always be the case: then the two slopes differ. Figure has been obtained from [4].*

Up to this point, all described phase changes have been from solid into liquid or vice-versa. Other phases can be used to store and release heat, but they are less suitable. Solid-solid, solid-gas or liquid gas phase changes exist. Phase changes involving a gas state have very high latent heats but they need very large volumes. Therefore gases are not very suitable for heat storage applications [3]. Solid-solid phase changes involve the transition of one crystalline to another. Due to the small latent heat, solid-solid phase changes are not very suitable for heat storage applications [3]. Phase changes from solid to liquid and vice versa are most suitable for heat storage systems [4].

An application of phase change materials is found in residential buildings. Space heating takes up the biggest part of energy consumption within a residential building: 53% [1]. Placing a phase change material in walls of the buildings may be a way to reduce energy consumption for space heating. Heat is stored during the day and released at night, exploiting the latent heat of the phase change material. Latent heat storage has two main advantages over sensible heat storage. First of all, the energy density of latent heat storage systems is higher. More heat can be stored in the same volume of storage material. Secondly, the phase change occurs at a constant temperature for pure substances, so temperature can be easily controlled when using a latent heat storage material [3].

Thermo-chemical heat storage (THS) is mainly determined by reaction kinetics [3]. To charge the system, heat is supplied to a chemical compound which will be called AB. There will be a chemical reaction that separates compound AB into compounds A and B. When the chemical reaction is a typical solid-gas reaction, the following process is utilized to charge the system:

$$\mathrm{AB(s)} + Q_{\mathrm{THS}} \rightarrow \mathrm{A(s)} + \mathrm{B(g)}$$

The heat that is required to separate compounds A and B from AB, is called reaction enthalpy, Q_{THS}. Once compounds A and B have been separated, they are stored in a separate environment. To discharge the system, compounds A and B are mixed to form compound AB again. The reaction is reversible and exothermic, so the reaction enthalpy is released as heat. Compounds A and B are called the sorbent and the sorbate respectively. Water vapor is often used as the sorbate and the sorbents can be a variety of materials.

For low temperature applications, often zeolite, silica gel and salt hydrates are used [5]. The energy density of THS storage media is approximately 8-10 times higher than SHS media and about twice as high as latent heat storage media [6]. Using this method of heat storage also enables the user to store heat for long periods of time [5]. Additional equipment is required, however. Air could be extracted from the environment, but then a humidifier is required to convert air to water vapor. Furthermore, a reactor is required to mix the water vapor with the sorbent. Efficient reactions are required to achieve the highest possible reaction heat. In order to have efficient reactions, heat -and mass transfer must be effective. This reduces the overall storage volume [6]. The additional equipment is relative expensive when compared to the price of a conventional hot water tank. Finally, the method of thermo-chemical heat storage is quite new and less mature than sensible -and latent heat storage [6].

Combining the electric hot water tank with additional equipment as humidifiers and reactors would increase the volume and complexity of the entire system. The aim of this project is to increase the heat capacity of the hot water tank without having to increase the total volume of the system. Therefore latent heat storage will be investigated in this report.

3 Phase Change Materials

The external storage medium consists of a latent heat based material, inside an annular space around the conventional hot water tank. Materials utilizing the effect of latent heat are called phase change materials (PCMs). Many different types of PCMs exist. In this chapter more information will be provided regarding the different types of PCM. After that, the most suitable PCM will be selected.

3.1 General Properties of Phase Change Materials

There are four thermal properties of PCMs having high impact on the final choice of a certain type of PCM: a suitable phase change temperature, latent heat, thermal conductivity and, to a lesser extend, the specific heat capacity of the PCM could also be taken into account [3]. These four properties are the following:

- Temperature of a suitable phase change may be the most important criterion. It will be the first step in narrowing down all sorts of PCMs. To fully exploit the latent heat storage, the phase change temperature should be in approximate range with operating temperatures of the system.
- The latent heat of a PCM should be as high as possible to maximize the energy density of the system. A very high latent heat also results in longer charging times and more required energy input.
- A low value of specific heat will lead to a higher diffusivity of the material. Heat will penetrate throughout the material faster. When the diffusivity is high enough, additional heat exchange surfaces or improving the thermal conductivity is not necessary.
- The thermal conductivity of the PCM should be as high as possible to increase the heat transfer rate from one medium to the PCM. In general the conductivity of PCMs is low. During solidification of PCM, the only mode of heat transfer is conduction through the solid material, which makes the process of solidification slow. Melting is a faster process because buoyancy effects will add to the conduction of heat through the PCM [4]. Many methods are investigated to increase the thermal conductivity of PCMs. This will be discussed in more detail later in this chapter.

The second set of properties that will be discussed are physical properties. Physical properties of a PCM consist of small vapor pressures at operating temperatures, small volume changes during the phase change and high density [3].

- Small vapor pressures of the PCMs are favorable, so that the rate of evaporation of the liquid state of the PCM is slow.
- Volume change of PCMs during phase change should be minimized. Some PCMs may undergo significant volume changes during a phase change, creating stresses in material surrounding the PCMs. One could use a smaller volume of PCM, but that will result in a decrease of heat storage capacity.
- High densities will provide for a greater amount of latent heat to be stored. A certain amount of volume will have a higher mass than a PCM with a lower density.

Kinetic properties are the third set of properties that will be discussed. They consists of the amount of sub-cooling, high nucleation rate and adequate rate of crystallization [3]. Since the amount of sub-cooling is determined by the nucleation rates and the rates of crystallization, they are all embedded into the sub-cooling process. Thus the only kinetic property of PCMs is the amount of sub-cooling.

- Sub-cooling could take place during the solidification of a PCM. Some PCMs will solidify at a temperature below their melting point. Instead of releasing latent heat, the temperature will decrease to the point that crystallization will initiate [4]. If no crystallization initiates, the material will only release sensible heat. [4]. Sub-cooling may occur if a PCM has a slow nucleation rate, a slow nuclei growth

rate or both. Encapsulated PCMs have an increased chance of undergoing sub-cooling, due to the small PCM volume inside the encapsulation [4]. Some techniques to reduce the amount of sub-cooling exist: addition of nucleating agents (seed crystals), applying the cold finger technique or using a rougher surface [4]. This paper will not get into detail regarding the solution methods. The interested reader is therefore referred to [4]. Figure 2 shows two processes of sub-cooling: the process on the left has no nucleation and a severe amount of sub-cooling. The process on the right shows a PCM which has been modified by adding seed crystals. There is only a small amount of sub-cooling.

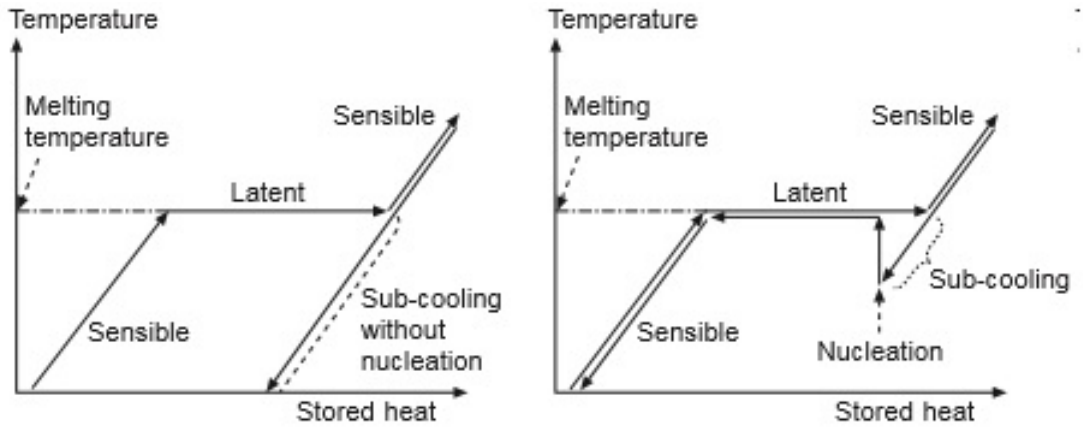

Figure 2: *Sub-cooling without addition of proper seed crystals (left). Sub-cooling with addition of proper seed crystals (right). Image obtained from [4].*

The next set of properties that will be discussed are the chemical properties: chemical stability, complete reversible freezing/melting cycle, compatibility with container materials and material properties as toxicity, flammability and explosivity [3].

- The chemical stability of a PCM should be high. A PCM should last for a large number of cycles (melting/solidification) without losing their performance and without changing thermal properties [4]. When a PCM is not chemically stable, the performance may decrease as time goes by.
- There should be complete reversible freezing/melting cycles within the PCM. For some PCMs incongruent melting will take place, which is an irreversible process. Incongruent melting happens when a hydrated salt separates into water and a lower hydrated salt [4]. The lower hydrated salt has a higher density than water, and it will sink to the bottom. This will result in only a small part of the top that will solidify when the temperature decreases [4]. Four methods to prevent incongruent melting exist: addition of suspension media/thickening agents, applying the extra water principle, chemical modification or dynamic melting. This paper will not go into detail explaining each improvement method. The interested reader is referred to [4].
- The PCM should be compatible with wall materials. When this is not the case, the wall and/or the PCM could be damaged and the lifetime of the system will decrease.
- The toxicity, flammability and explosivity of PCMs should be minimized wherever possible for safety reasons.

Finally, the economical properties of PCM's will be presented. These include: effective costs and large scale availability [3].

- Effective costs should be minimized. Effective costs will consist of material costs, maintenance costs, but also costs for additional components.

- Large scale availability will help reduce the material costs. Furthermore, a depletion of material will be less likely when the material is available on a large scale.

3.2 Classification of Phase Change Materials

Now that the different properties of the PCMs have been distinguished, it is possible to assign the different properties to the different types of PCMs. A distinction has been made between organic PCMs, inorganic PCMs and eutectics. The organic class of PCMs is subdivided into two main categories: paraffin compounds and non-paraffin compounds.

Paraffin compounds consist of long chains n-alkanes of the form $CH_3 - (CH_2) - CH_3$. A longer chain results in a higher melting point and a higher value for the latent heat [3,7]. Paraffin compounds are known to be safe, reliable and non-corrosive [3,7]. Their behaviour is predictable [3]. Below temperatures of 500 °C, the paraffin based compounds are stable and inert: they are suitable for performing long times without degradation of its properties. Vapor pressures are low at operating temperatures and there is no incongruent melting [7]. No to a little sub-cooling takes place [3]. A large temperature range exist for the phase change: 5-80 °C [3]. Finally, the paraffin compounds are recyclable [3].

In pure form, the paraffin compounds are very expensive [3,7,8]. The industrial grade paraffin compounds are cheap, but their properties may not be the same as pure paraffin compounds. Often these industrial grade paraffins are a mixture and therefore they have no melting point, but a melting range. The latent heat of paraffin compounds is relatively low [3]. Furthermore, the thermal conductivity of paraffin compounds is very low compared to other types of PCMs. They are moderately flammable and they can't be used in combination with plastics [7]. Volume changes of paraffin compounds are large compared to other types of PCMs [3].

Non-paraffin compounds can be a great variety of different compounds: esters, fatty acids, alcohols and glycols. Their properties may differ from one type to another type. In general, they have higher latent heat values when compared to paraffin based compounds and most of them are inflammable [3,7].

However, they have a low thermal conductivity and they are not stable at high temperatures [3,7]. They can also be toxic [7]. Among non paraffin compounds, fatty acids attract the attention of specialists [8]. They have high latent heats compared to paraffin based PCMs and show little to no sub-cooling. However, they are more expensive than paraffin compounds (2-2.5 times more expensive), they have an unpleasant odor and they are mildly corrosive [3,7].

Inorganic PCMs are also divided into separate classes: salt hydrates and metallics. Salt hydrates have the form $S \cdot nH_2O$. S represents an inorganic salt. Salt hydrates have higher latent heats and higher values of thermal conductivity than the organic PCMs [3,7]. They show little corrosion (but more than organic PCMs) and they are compatible with plastics, unlike organic PCMs [3]. Their volume change is smaller than the volume change for organic PCMs [7]. They are not very expensive compared to other types [7].

However, as previously mentioned, incongruent melting could occur when using salt hydrates. They also show a high degree of sub-cooling [3,7,8]. At high temperatures they tend to get unstable [3,8], while at low temperatures they may freeze [3]. A lot of maintenance is required when dealing with salt hydrates [3].

Metallics consist of low melting temperature metals and their alloys. They are suitable for high temperature applications [3] and their thermal conductivities are high [3,7]. The vapor pressures of metallics are low [7]. The latent heat per unit mass is low, but since the densities of metallics are high in general, the latent heat per unit volume is high. This will, however, result in very heavy equipment [7].

Eutectics are a combination of two or more PCMs with similar (congruent) melting and freezing points. They can be a combination of two organic PCMs, two inorganic PCMs or a combination of both. By varying the weight fraction of one PCM, the melting point is variable. For this reason they are a great promise to the future: the melting temperature can be controlled [3]. They have high conductivities and no segregation occurs. Also, their densities are high [3]. However, they have low latent heat of fusion in general [3].

3.3 Motivation for Selecting Optimal PCM

In this section, the PCM that is most suitable for the application in a domestic hot water tank will be

made. The choice will depend on the importance of different properties for our application.

The PCM in our application will be placed in an annulus between two copper cylinder walls, since this is easy to implement in already existing hot water tanks. The melting temperature should be as close to 60.0 °C as possible, since this will be the approximate maximum temperature in the tank. The PCM should be cheap and to reduce the system volume, the latent heat per unit volume should be as high as possible. The thermal conductivity should be high because this will result in high charging- and discharging rates. One of the most important aspects is the lifetime of the PCM: since a conventional hot water tank has an average lifetime of 10-15 years, many thermal cycles will take place. The PCM should be able to deal with many cycles without losing its thermal properties and it should remain stable.

Some PCM's have been collected in table 1 with suitable melting temperatures. Sometimes certain properties are not available, these are denoted by a - sign. Eutectics are shown with the mass weight percentage for each element inside the eutectic. The (s) and (l) signs mean for solids and liquids respectively.

Name	Class	T_m (°C)	L (kJ/kg)	c_p (kJ/(kgK))	k (W/(mK))	ρ (kg/m^3)	Source
Paraffin 57 (Russia)	Paraffin Compound	57 ± 2	98	-	0.7	-	[8]
RT 60 Rubitherm	Paraffin Compound	58-60	214	930	0.2	850 (s) 775 (l)	[8]
Palmitic Acid	Non-Paraffin Compound	61.0	222	1690 (s) 2200 (l)	0.21 (s) 0.17 (l)	989	[3]
Heptaudecanoic Acid	Non-Paraffin Compound	60.6	189	-	-	-	[7]
$CH_3COONa \cdot 3H_2O$	Salt Hydrate	58	265	1680 (s) 2370 (l)	0.43 (s) 0.34 (l)	1450	[3]
$Fe(NO_3)_2 \cdot 6H_2O$	Salt Hydrate	60.5	126	-	-	-	[7]
Cerro-low Eutectic	Metallic	58.0	90.9	-	-	-	[3]
Bi Cd In Eutectic	Metallic	61.0	25.0	-	-	-	[3]
$Mg(NO)_3 \cdot (H_2O)_6$ (59 wt%) + $MgCl_2 \cdot (H_2O)_6$ (41 wt%)	Eutectic	59	132	2290 (s) 2810 (l)	0.670 (s) 0.530 (l)	1610	[3]
$Mg(NO_3)_3 \cdot 6(H_2O)$ (53 wt%) + $Al(NO_3)_2 \cdot 9(H_2O)$ (47 wt%)	Eutectic	61.0	148	-	-	-	[7]

Table 1: *Some selected PCMs in the applicable temperature range (58.0 °C - 61.0 °C)*

The melting temperature inside table 1 is denoted by T_m and the latent heat is presented by L. The sign c_p stands for the specific heat capacity of the PCM and k represents the thermal conductivity. The density of PCM's is denoted by ρ.

Since salt hydrates are mildly corrosive, the option to use a salt hydrate has been disregarded. A combination of copper walls with a salt hydrate could decrease the performance of the system, resulting in a shortened lifetime of the hot water tank. Furthermore, incongruent melting and sub-cooling could occur, which would have a negative impact on the overall thermal performance of the PCM. Using metallics could be an option, but their latent heats are low compared to the organic PCMs and eutectics: with the same amount of mass, less heat could be stored as latent heat. Also eutectics have smaller latent heat than the organic PCMs, so eutectics have been disregarded as an option. Thermal properties of non-paraffin compounds and paraffin compounds are comparable. However, since non-paraffin compounds are more expensive than paraffin compounds, the choice has been made to use a paraffin compound. RT 60 Rubitherm has higher latent heat than paraffin 57. Therefore, the final choice for the PCM in this report is RT 60 Rubitherm. It will be safe, reliable and non-corrosive. For our application it will not get in contact with plastics. Sub-cooling and incongruent melting are absent and it remains stable for long periods of time.

Two major drawbacks arise when using RT 60 Rubitherm as a PCM: the large volume changes and the low thermal conductivity. Many solutions exist to increase the thermal conductivity of paraffin based PCMs. These solutions will be discussed in the next section. The volume change will be neglected throughout this report to simulate an ideal case where a maximum volume of PCM is used in both liquid and solid phases.

3.4 Methods to Increase Thermal Conducitity of Phase Change Materials

At this point, a suitable PCM has been chosen: RT 60 Rubitherm. As mentioned in the previous section, the thermal conductivity is low and to achieve maximal performance, the thermal conductivity should be increased. Much research has been performed on methods to increase the thermal conductivity of PCMs. For brevity these methods will not be discussed in this current paper. The most popular methods will be

outlined in short. Some more detail will be provided regarding the most suitable method for the remainder of this thesis paper.

One of the simplest methods to increase the thermal conductivity of the PCM is to disperse nano- or micro-sized high conductive particles into the PCM. Both high- and low density materials can be dispersed. Research on high density particles included copper nanoparticles [9], aluminum nanoparticles [10] and aluminum microparticles [11]. The major drawback is their high density. For particles with a large diameter, there may be rapid settling to the bottom of the tank. Assuming small particle Reynolds numbers, the settling velocity for spherical particles can be calculated by balancing the buoyancy force and the opposing stokes drag force:

$$\frac{\pi(\rho_p - \rho_f)g d_p^3}{6} = 3\pi\mu_f d_p u_s \tag{4}$$

In this equation ρ, g, d, μ and u_s represent the density, gravitational acceleration, diameter, dynamic viscosity and settling velocity respectively. Subscripts p and f represent particle and fluid respectively. The settling velocity can then be evaluated after rewriting this balance:

$$u_s = \frac{(\rho_p - \rho_f)g d_p^2}{18\mu_f} \tag{5}$$

Using large high density particles may result in rapid settling velocities and so one should minimize the particle diameter as much as possible. Apart from taking very small particles, another solution to tackle the settling problem would be to use low density materials. Carbon fibres have a low density and a heat conductivity that is comparable with aluminum. Furthermore, they are compatible with most types of PCMs and have a high resistance to corrosion [3]. By changing the shape of the carbon fibres and the grade of homogeneity, the conductivity can be increased [12,13].

Another method is to use a composite of PCM with a higher conducting porous material. Expanded graphite could be used as porous structure in combination with PCMs [14]. It is also possible to use a metal foam instead of expanded graphite. Aluminum was used in [15]. A combination of both methods may be used, as has been done in [16]. The increase of thermal conductivity when using porous materials is highly dependent of porosity and pore size. An optimal balance must be sought [15]. Using expanded graphite could lead to PCM leakage and material instabilities during phase change [14]. Furthermore, it is quite an expensive process to convert graphite into expanded graphite.

Encapsulation of PCMs is another method to enhance thermal conductivity. The capsules can be macro-, micro- or nano-sized. By using capsules, one increases the surface area over volume ratio which enhances heat transfer. The smaller the capsules, the more impact this effect will have. Furthermore, there is no leakage of PCM into the environment due to the encapsulation. This allows the user to also select PCMs which may be corrosive with the environment. In order to prevent leakage, however, one must take into account the volume change of the PCMs or use a flexible material. Often polymers are used due to their flexibility, but it is also possible to use inorganic shells such as silica. Silica has a higher conductivity than polymers, but it is also more brittle. Composites of both polymer and silica are also used to exploit advantages of both materials [17].

Many other methods to increase the thermal conductivity exist, such as increasing heat transfer surface by using fins or using pipes. For more information about these methods, the reader is referred to [3].

In this report the PCM conductivity was enhanced by dispersing nano-sized alumina particles. This is a cheap solution and easy to implement into any future experiment. Furthermore, it allows us to calculate the PCM composite properties by using volume fractions of PCM and alumina. The major drawback of alumina is its high density and therefore its rapid settling to the bottom of the tank for large particles. This may cause trouble for long terms applications, but in scope of this report, if the particles are small enough, this phenomenon can be ignored, as will be shown in the following calculation: let's assume that $\rho_f = 900$ kg/m^3, $\rho_p = 2700$ kg/m^3, $\mu_f = 20$ mPa·s. These are some properties obtained from [34] where a similar PCM is used as the PCM that will be selected in this report. some rough calculations can be made for the settling velocity using the balance of the buoyancy and stokes drag force. For particles with $d_p = 1.0$ μm, the settling velocity will be approximately $u_s = 4.9 \cdot 10^{-8}$ m/s. For particles with diameter $d_p = 1.0$ nm, the

settling velocity will be $u_s = 4.9 \cdot 10^{-14}$ m/s. These velocities are very small, and the time to settle will be very large. Therefore, the effect of rapid settling is negligible. Furthermore the effect of Brownian motion (random movement of the dispersed particles) on the thermal properties is ignored to simplify the process of calculating thermal properties. Given a volume fraction (e) of particles over PCM, the properties of the composite are calculated using the following equations [9]:

$$\rho_{\text{mix}} = (1-e)\rho_{\text{pcm}} + e\rho_p \tag{6}$$

$$\mathrm{c}_{\mathrm{p}_{\text{mix}}} = \frac{(1-e)(\rho \mathrm{c}_{\mathrm{p}})_{\text{pcm}} + e(\rho \mathrm{c}_{\mathrm{p}})_p}{\rho_{\text{mix}}} \tag{7}$$

$$L_{\text{mix}} = \frac{(1-e)(\rho L)_{\text{pcm}}}{\rho_{\text{mix}}} \tag{8}$$

$$k_{\text{mix}} = k_{\text{pcm}}\left(\frac{1-2e\kappa}{1+e\kappa}\right) \tag{9}$$

where conductivity ratio κ is defined as

$$\kappa = \frac{k_{\text{pcm}} - k_p}{k_p + 2k_{\text{pcm}}} \tag{10}$$

The volume fraction has been obtained using

$$e = \frac{V_p}{V_{\text{pcm}}} = \frac{m_p}{\rho_p V_{\text{pcm}}} \tag{11}$$

The volume of PCM was calculated from the tank dimensions (see table 4). The volume change of PCM was neglected. The added mass of (pure) aluminum was 500 grams (leading to a volume fraction of $e \approx 0.011$). Adding more aluminum only results in a negligible increase in conductivity, while the value of latent heat decreases. The values of the specific heat capacity and latent heat are approximately equal in solid and liquid state for the mixture. For the density of the composite, the average value has been taken between solid and liquid. The properties of aluminum, RT 60 Rubitherm and the composite are shown in table 2.

	Aluminum	RT 60 Rubitherm	Composite
ρ [kg/m^3]	2702	830(s) 775(l)	851(s) 796(l)
$\mathrm{c_p}$ [J/(kgK)]	903	930	929
L [kJ/kg]	-	214	206
k [W/(mK)]	273	0.2	1.03

Table 2: *Different properties of Alumina, RT 60 Rubitherm and the composite. Property changes for the mixture between solid-and liquid phase are very small and thus neglected.*

The conventional hot water tank will have a diameter of 40 cm and a height of 30 cm to approximately match the dimensions of a small sized domestic hot water tank. The PCM-enhanced hot water tank will have the same dimensions, but the outer layer will consist of 5.0 cm PCM instead of water. The resulting masses, volumes and energy capacities are shown in table 3. These values are based on a temperature difference of 50.0 °C and 4.18 kJ/kg as the specific heat capacity of water. Both sensible and latent heat were taken into account for the PCM-enhanced hot water tank.

	Conventional hot water tank	PCM-enhanced hot water tank
V_w	37.7 L	21.2 L
V_{pcm}	0 L	16.5 L
m_w	37.3 kg	21.0 kg
m_{pcm}	0 kg	13.6 kg
E	7.8 MJ	7.8 MJ

Table 3: *Volumes, masses and energy capacities of the two different tank types.*

One major drawback of defining both systems in this way is that the energy capacity per unit volume does not increase: 7.8 MJ can be stored in both tanks within the same volume. However, these calculations are based on a temperature difference of 50.0 °C: heating from 20.0 °C to 70.0 °C. In reality this temperature difference may be smaller, leading to an increase in heat capacity for the PCM-enhanced hot water tank. For example, if the maximum temperature in the system would be 60.0 ° C, the heat capacity of the PCM-enhanced hot water tank would be increased by 9.1% compared to the conventional hot water tank. However, to increase the melting rate of PCM, the maximum temperature has been set to 70.0 °C in the remainder of this report.

4 Hot Water Storage Tanks

In this section, a short outline will be given regarding hot water storage tanks in general and already existing models of hot water storage tanks. At the end of the section, the most appropriate model will be chosen and then used in the remainder of this thesis paper.

Whenever hot water of a uniform temperature is stored inside water tanks, eventually stratification will occur inside the tank. Since heat losses at the top are generally higher than at the bottom, the water at the top will cool down. Due to the density difference of cold and hot water, cold water will sink and hot water will rise. Layers of different temperature will coexist and it is said that the tank is (thermally) stratified. Obviously, when a cold water flow is introduced (during the discharge cycle), in a tank of uniform temperature, stratification will occur. Different levels of stratification may exist as is shown in figure 3.

An important aspect of a stratified tank is the thermocline. The thermocline is the region inside the tank where the steepest temperature gradient exists. A perfectly stratified tank has no thermocline, because the temperature gradient is infinite. In reality, there is always a thermocline present. The smaller the thermocline, the higher the level of stratification. If a tank is fully mixed, there is no temperature gradient at all and there is no stratification. The different existing models will be discussed as well as their assumptions and simplifications. The novelty in this report is the addition of PCM around the hot water tank.

In general, performance of systems with a high level of stratification is higher than fully mixed systems [19,20]. In order to increase the performance of hot water tanks, the level of destratification should be minimized. There are four major contributors to destratification: heat losses to the ambient, axial heat diffusivity of water, vertical conduction through the tank walls and introduction of mixing during a charge/discharge cycle [20]. Note that for water, diffusivity throughout the tank is small. Using hot water tanks which are very well isolated also excludes the destratification due to ambient losses. Thus, the two major contributors to destratification are wall conduction and mixing that is introduced by an inflow and outflow of water with a different temperature.

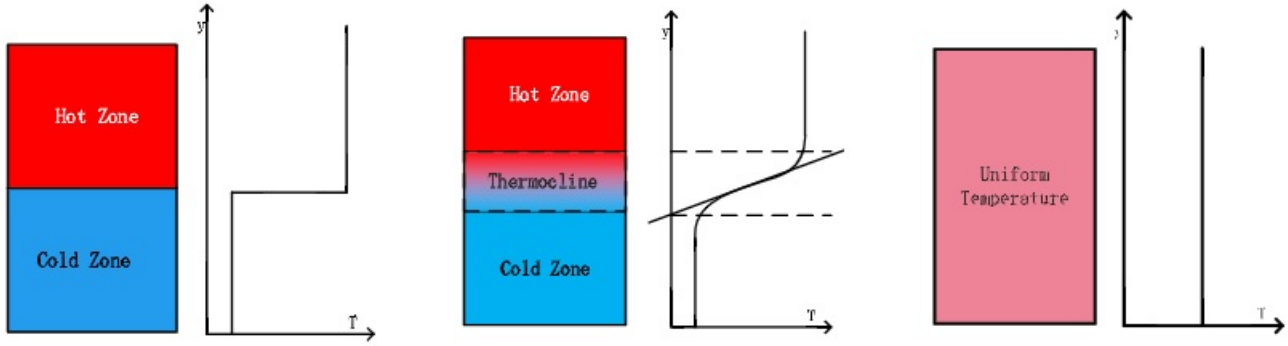

Figure 3: *From left to right: perfectly stratified, moderate level of stratification, no stratification. Figure obtained from [18].*

Kleinback et al. compared two different 1-D storage tank models for solar domestic hot water tanks: a multinode model and a plug flow model. In the multinode model the tank was divided into N axial segments, all perfectly mixed. Differential equations were written for each segment and solved. The plug flow model was based on the displacement of a certain volume of water entering the tank. The same amount of volume left the tank at the same time, and a new temperature was introduced at the location where flow entered the tank. Also a plume entrainment model was implemented into the plug flow model. Correlations were required to couple the plume region to the tank region. The 1-D model was then solved using the finite difference method. The fully mixed tank model turned out to under-predict the temperature and the plug flow model turned out to be more accurate than the multinode model. However, it tended to over-predict the energy contents [20].

Zurigat et al. extended the multinode 1-D model to an effective diffusivity model where an effective diffusivity term was added to the 1-D equations to account for turbulent mixing at the inlet. Experiments were performed for three different types of inlet: the side inlet, a perforated inlet and an impingement inlet. Correlations to determine the additional diffusivity were obtained as a function of the inlet Reynolds- and Richardson number for the three different inlet types. The effective diffusivity model turned out to be in good agreement with existing experiments. When the Richardson number exceeded the value of 3.6, the influence of the inlet geometry on stratification became negligible. Thus, when dealing with inlet flows having a Richardson number below 3.6, Zurigats correlations could be used to take into account the mixing effects [21].

Nizami et al. developed a quasi 1-D model. The plume region was subdivided into three smaller regions. Between the tank top and jet penetration depth, the model also had a radial component in the system, due to the temperature difference of the jet and the remainder of the tank. For each region differential equations were set up and correlations were obtained from the CFD program ANSYS-CFX-12.0. The mixing was mainly dominated by the penetration depth. The penetration depth of the jet turned out to be a function of the Richardson number and the inlet pipe diameter. There was good agreement with the CFD-simulations [22].

K.E. Torrance used a vorticity-stream method to solve a 2-D axisymmetric case: a cylinder that was heated from below. Transient natural convection was investigated. Five different finite difference schemes were introduced and compared. Some of these methods were explicitly solved, others implicitly. Some of these methods conserved vorticity and energy, while other methods didn't. All of these methods had a restrictive time-step. Finally, some of these methods introduced false viscosity and convection, and these methods should be handled with care: the mesh size can't be too large [23].

In another report, K.E. Torrance and J.A. Rockett then used one of the methods from [23] to solve the problem of natural convection inside an axisymmetrical enclosure. They did simulations for the Grashoff range $4 \cdot 10^4$ - $4 \cdot 10^{10}$. Excellent agreement was obtained with experiments up to a Grashoff number of $1.2 \cdot 10^9$ [24].

E. Hahne and Y. Chen used the vorticity stream function method to solve for temperature and flow characteristics during the charging cycle for a hot water tank. The influence of inlet velocities, charging temperature differences, charging flow rates and tank height to diameter ratios on charging efficiency were investigated. The charging efficiency was based on evaluating the thermal stratification inside the tank. They showed that charging efficiency highly depends on the Richardson- and Peclet number. For Richardson numbers below 0.25, the charging efficiency was higher than 97%. Furthermore, increasing the Peclet number also increases the charging efficiency, given a fixed value of the Richardson number. Finally, for height to diameter ratios smaller than 4, the charging efficiency can be increased by increasing this ratio. Correlations were obtained for the charging efficiency [25].

L. Cai and W.E. Steward used a turbulent mixing model to simulate a lower corner inlet flow. The vorticity stream formulation was extended with an equation for turbulent kinetic energy and a turbulent length scale. They concluded that for an Archimedean number below 5, and a Reynolds number below 1000, the cold fluid will not extensively mix with warmer fluid in the tank. The warm and cold fluids will thermally stratify under these conditions [26].

The streamfunction-vorticity method will be used from Torrance and Rockett to model the charging model, since this method is suitable for 2-D axisymmetric problems. Their finite discretization scheme conserves energy and vorticity, has no spatial mesh size restriction and is very stable but it introduces numerical viscosity and diffusivity. Therefore, a very fine mesh is required to approximate the governing equations, while the computational effort should be minimized. The discharging model is modeled by using the equations used by Hahne and Chen, with a finite difference scheme from Torrance. This scheme has a divergent free velocity field, unlike the method from Torrance and Rockett, which resulted in oscillations around $r = 0$ for the discharge cycle in this report. The discretization method is second order accurate reducing numerical diffusivity and viscosity. More detailed information will be given in the section results.

5 Modeling of PCM Enhanced Hot Water Boiler

In this section, a 2-D model for the PCM-enhanced hot water tank is presented. Both charging- and discharging of the tank will be discussed. First, the geometry is defined for the system, then the governing equations for each cycle, initial- and boundary conditions and their implementation in MATLAB.

5.1 Charging Model

The geometry of the system during the charging cycle is defined as presented in figure 4. The geometry of the system for the discharging cycle is slightly different and is shown in figure 6. The total height of the tank is h. The axis of symmetry is located at $r = 0$. The interface between water and PCM is located at $r = r_i$ and the outer wall of the cylinder is defined at $r = r_o$. The term q represents volumetric heating and this term is assigned to specific nodes representing the electrical resistor. The electrical resistor is situated at the center of the tank to match the geometry of a real domestic hot water tank (provided by Inventum). Furthermore, it the symmetry of the system can be used when placing the heater at the center of the tank. More detail on the electric heater will be provided later in this section. The number of nodes in radial direction are denoted by n_r for the water and n_{pcm} for the PCM. The number of axial nodes is denoted by n_z. Subscript i represents the axial nodal position so that $z = i\Delta z$. Subscript j represents the radial nodal position so that $r = j\Delta r$.

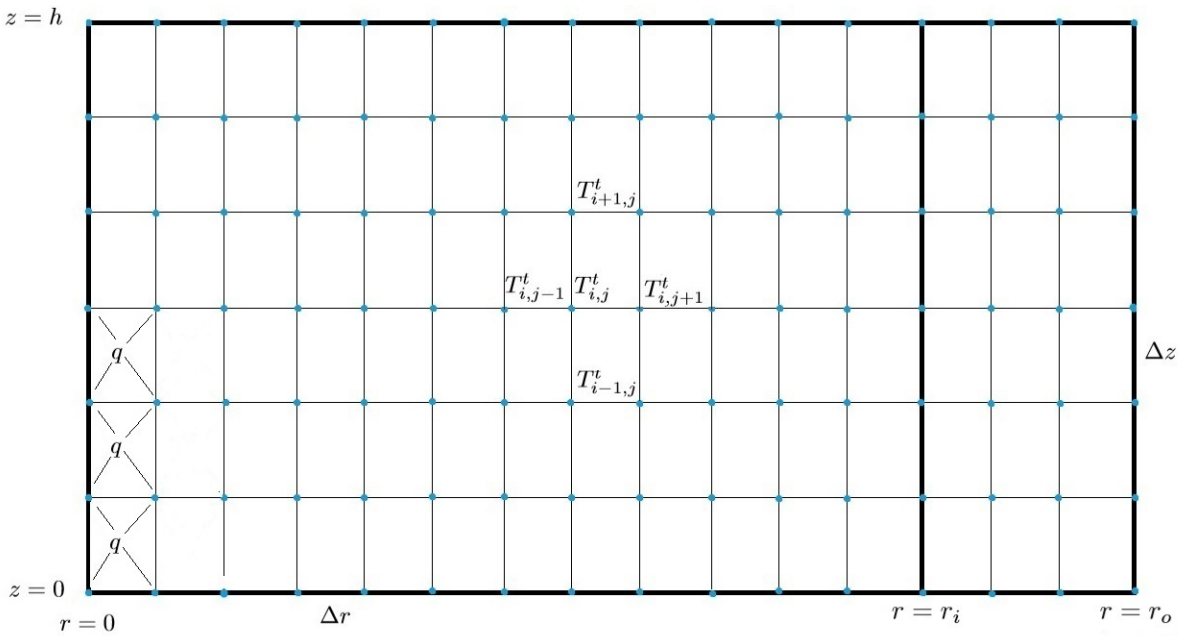

Figure 4: *System geometry for simulating the charging cycle. The nodes that have a 'q' assigned to them are generating the heat during the charging cycle.*

5.1.1 Governing Equations

The governing equations have been adapted from [24]. The vorticity-stream function method to solve the governing equations (continuity, momentum and energy) is used. The system is assumed to be axisymmetric and viscous heating has been neglected. Furthermore, the Boussinesq approximation has been used. The Boussinesq approximation allows us to use constant values for the density during the simulation, except for the term that is driving the flow due to the density difference. By defining the vorticity as being the curl of

the velocity vector,

$$\Omega = \frac{\partial v}{\partial z} - \frac{\partial u}{\partial r} \tag{12}$$

and by introducing the stream function Ψ of the flow, the two momentum equations for the r-and z-components are converted into one vorticity equation. Continuity is satisfied automatically by definition of the stream function. The following dimensionless parameters (without an asterisk) are introduced to model the charging cycle of the hot water tank:

$$t = \frac{\alpha}{h^2}t^* \quad z = \frac{z^*}{h} \quad r = \frac{r^*}{h} \quad v = \frac{h}{\alpha}v^* \quad u = \frac{h}{\alpha}u^* \quad T = \frac{T^* - T_o}{T_h - T_o} \tag{13}$$

For clarity, the dimensionless parameters are without an asterisk from now on. The thermal diffusivity of water is denoted by α and h is a characteristic length scale (the tank height). Temperatures T_o and T_h are the initial and maximum temperature of the system during the simulation. The velocities v and u are the dimensionless radial and axial velocities respectively. The dimensionless parameters are substituted into the governing vorticity-stream-temperature equations, and the following set of equations has been obtained for the water region ($0 \leq r \leq r_i$):

$$v = -\frac{1}{r}\frac{\partial \Psi}{\partial z} \quad u = \frac{1}{r}\frac{\partial \Psi}{\partial r} \tag{14}$$

$$\frac{1}{r}\frac{\partial^2 \Psi}{\partial z^2} + \frac{\partial}{\partial r}\left(\frac{1}{r}\frac{\partial \Psi}{\partial r}\right) = -\Omega \tag{15}$$

$$\frac{\partial T}{\partial t} + \frac{\partial (uT)}{\partial z} + \frac{1}{r}\frac{\partial (rvT)}{\partial r} = \frac{\partial^2 T}{\partial z^2} + \frac{1}{r}\frac{\partial}{\partial r}\left(r\frac{\partial T}{\partial r}\right) + \epsilon\sigma \tag{16}$$

$$\frac{\partial \Omega}{\partial t} + \frac{\partial (u\Omega)}{\partial z} + \frac{\partial (v\Omega)}{\partial r} = -\mathrm{GrPr}^2\frac{\partial T}{\partial r} + \mathrm{Pr}\left[\frac{\partial^2 \Omega}{\partial z^2} + \frac{\partial}{\partial r}\left(\frac{1}{r}\frac{\partial (r\Omega)}{\partial r}\right)\right] \tag{17}$$

These equations will be referred to as the velocity equation, stream function equation, temperature- and vorticity equation respectively. Three dimensionless numbers characterize the flow: the Prandtl number Pr, the Grashof number Gr and a term which takes into account the volumetric heating σ. They are defined as:

$$\sigma = \frac{qh^2}{k(T_h - T_o)} \quad \mathrm{Pr} = \frac{\nu}{\alpha} \quad \mathrm{Gr} = \frac{g\beta(T_h - T_o)h^3}{\nu^2} \tag{18}$$

The Prandtl number is the ratio of the viscous diffusion over thermal diffusion and the Grashof number is the ratio of buoyant forces over viscous forces. The term inside the vorticity equation containing $-\mathrm{GrPr}^2$ is a buoyancy source term which has been added to the equations to drive the flow. This term accounts for the density difference. For a detailed derivation of this term, the reader is referred to appendix C. The heater is assumed to be a cylindrical volume. For the controlling parameter ϵ, a value of 1 has been assigned to the nodes which contain the fictitious heating element. For all other nodes, the value has been set to 0.

The equations are in conservative form: the nodes are fixed in space (an Eularian frame of reference). Mathematically these equations are the same as the equations written in non-conservative form, but the discretization process is different for both methods. The advantage of using a conservative form of the equations is that when one adds all interior grid points in one direction, only the boundary terms remain because all interior nodes cancel each other. Using the non-conservative form adds new terms when adding grid points, since none of the terms cancel inside the interior.

The governing equations for the PCM region, $r_i \leq r \leq r_o$, differ from those inside the water region. For the PCM, only thermal diffusion has been taken into account. Furthermore, the usual dimensional equations are used instead of the nondimensional equations. The motivation to do so is based on the fact that if we were to nondimensionalize the PCM heat equation, a different time scale will arise than for the water region. To model the phase change inside the PCM, an explicit enthalpy method has been adapted from [27]. In

this method, first the enthalpy is evaluated for each PCM node using the heat diffusion equation. To rewrite the diffusion equation from temperature to specific enthalpy, the assumption has been made that the specific heat capacity does not depend on temperature, thus:

$$H = \mathrm{c_{p_s}} T_s \tag{19}$$

The governing equation for the PCM then becomes the following:

$$\frac{\partial H}{\partial t} = \frac{k_s}{\rho_s}\left(\frac{\partial^2 T_s}{\partial z^2} + \frac{1}{r}\frac{\partial}{\partial r}\left(r\frac{\partial T_s}{\partial r}\right)\right) \tag{20}$$

The thermal conductivity and density of the PCM are denoted by k_s and ρ_s respectively. Once the values of the specific enthalpy H have been obtained, the following relation is used to convert to temperature:

$$T_s = \begin{cases} T_m + (H/\mathrm{c_{p_s}}) & H < 0 \\ T_m & 0 \leq H \leq L \\ T_m + (H-L)/\mathrm{c_{p_s}} & H > L \end{cases} \tag{21}$$

The melting temperature is given as T_m and L is the value of the latent heat of the PCM material.

5.1.2 Boundary - and Initial Conditions

To solve all governing equations, boundary-and initial conditions are required. They are presented all together for clarity. Note that due to non-dimensionalizing the term r_i is defined as: $r_i = r_i^*/h$. A more detailed explanation of the boundary conditions follows after defining them:

$$\Psi = \Omega = \frac{\partial T}{\partial r} = 0 \quad r = 0 \quad 0 \leq z \leq 1 \tag{22}$$

$$T = T_s \quad -k\frac{\partial T}{\partial r} = -k_s\frac{\partial T_s}{\partial r} \quad \frac{\partial \Psi}{\partial r} = \Psi = 0 \quad r = r_i \quad 0 \leq z \leq 1 \tag{23}$$

$$\frac{\partial T_s}{\partial r} = 0 \quad r^* = r_o^* \quad 0 \leq z^* \leq h \tag{24}$$

$$\frac{\partial \Psi}{\partial z} = \Psi = 0 \quad \frac{\partial T}{\partial z} = 0 \quad z = 1 \quad 0 \leq r \leq r_i \tag{25}$$

$$\frac{\partial T_s}{\partial z} = 0 \quad z^* = h \quad r_i^* \leq r^* \leq r_o^* \tag{26}$$

$$\frac{\partial \Psi}{\partial z} = \Psi = 0 \quad \frac{\partial T}{\partial z} = 0 \quad z = 0 \quad 0 \leq r \leq r_i \tag{27}$$

$$\frac{\partial T_s}{\partial z} = 0 \quad z^* = 0 \quad r_i^* \leq r^* \leq r_o^* \tag{28}$$

The axis of symmetry can be seen as a single streamline on which we assign the value of 0. Due to symmetry it is found that $\partial f/\partial r = 0$ where f can be any parameter. Also zero vorticity exists at the axis of symmetry because the radial velocity is zero: $v = 0$. Then by definition of vorticity, it is found that

$$\Omega = -\frac{\partial u}{\partial r} \tag{29}$$

Since all derivatives in r-direction are zero in the axis of symmetry, it is indeed found that $\Omega = 0$. At solid walls, the no-slip boundary condition is applied: there is no tangential and radial velocity component present ($u = v = 0$). The walls are assumed to be perfectly insulated. At the intermediate wall at $r = r_i$, an inter-facial boundary condition has been applied. It is assumed that there is perfect thermal contact since two layers of copper have very little thermal resistance. Initially, all temperatures are equal to T_o, and there is no flow in the system:

$$\Psi = T = \Omega = 0 \quad t = 0 \quad 0 \leq z \leq 1 \quad 0 \leq r \leq r_i \tag{30}$$

$$T_s = T_o \quad t^* = 0 \quad 0 \leq z^* \leq h \quad r_i^* \leq r^* \leq r_o^* \tag{31}$$

5.1.3 Discretization Method for Water Region

Special attention is given to the nonlinear derivatives (or the convection terms). According to [24], stability of these nonlinear terms is conserved by using a special 3 point non-central difference method which is defined as:

$$\left(\frac{\partial(uf)}{\partial z}\right)_{i,j} = \frac{\bar{u}_1^t f_{i,j}^t - \bar{u}_2^t f_{i-1,j}^t}{\Delta z} \quad \bar{u}_1^t \geq 0 \quad \bar{u}_2^t \geq 0 \tag{32}$$

$$\left(\frac{\partial(uf)}{\partial z}\right)_{i,j} = \frac{\bar{u}_1^t f_{i+1,j}^t - \bar{u}_2^t f_{i,j}^t}{\Delta z} \quad \bar{u}_1^t < 0 \quad \bar{u}_2^t < 0 \tag{33}$$

$$\left(\frac{\partial(uf)}{\partial z}\right)_{i,j} = \frac{u_{i+1,j}^t f_{i,j}^t - u_{i-1,j}^t f_{i,j}^t}{2\Delta z} \quad \bar{u}_1^t \geq 0 \quad \bar{u}_2^t < 0 \tag{34}$$

$$\left(\frac{\partial(uf)}{\partial z}\right)_{i,j} = \frac{\bar{u}_1^t f_{i+1,j}^t - \bar{u}_2^t f_{i-1,j}^t}{\Delta z} \quad \bar{u}_1^t < 0 \quad \bar{u}_2^t > 0 \tag{35}$$

The term f can both be θ or Ω. The velocities containing a bar, are averaged velocities between two grid points, defined as:

$$\bar{u}_1^t = \frac{u_{i+1,j}^t + u_{i,j}^t}{2} \quad \bar{u}_2^t = \frac{u_{i,j}^t + u_{i-1,j}^t}{2} \tag{36}$$

The nonlinear term containing the radial velocity is discretized in the same manner, but then $\bar{u}_1^t$ and $\bar{u}_2^t$ terms are replaced by their radial counterparts $\bar{v}_1^t$ and $\bar{v}_2^t$, which are defined as:

$$\bar{v}_1^t = \frac{v_{i,j+1}^t + v_{i,j}^t}{2} \quad \bar{v}_2^t = \frac{v_{i,j}^t + v_{i,j-1}^t}{2} \tag{37}$$

A schematic of the positions of these mean velocities is shown in figure 5. Also a system view from above has been shown for clarity.

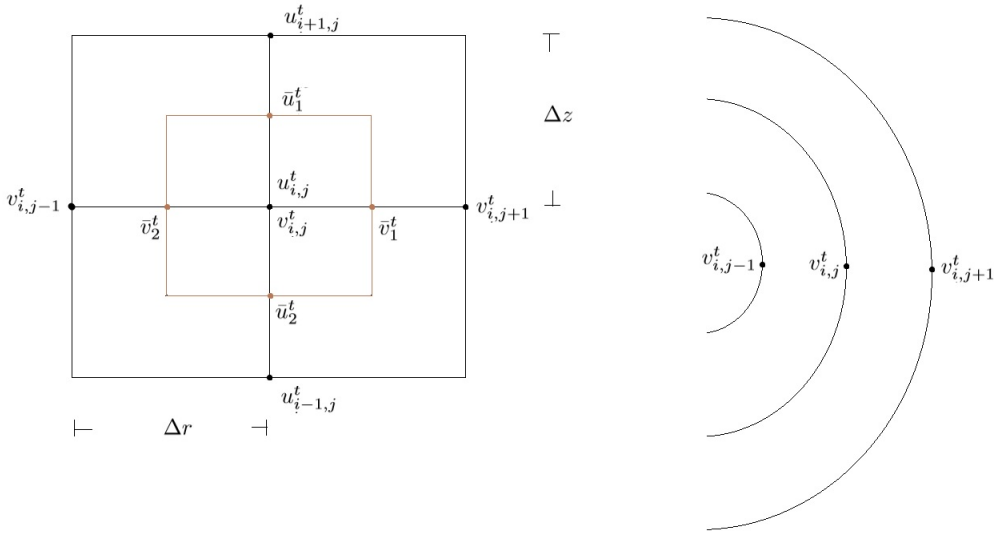

Figure 5: *Positions of mean velocities $\bar{u}_1^t$, $\bar{u}_2^t$, $\bar{v}_1^t$ and $\bar{v_2}^t$ (left). System schematic from above: the tank is divided into equidistant rings having a radial thickness of Δr and an axial thickness of Δz (right).*

All terms from the governing equations are integrated over a small cylinder of height Δz and radius Δr to obtain the finite difference schemes (except at the center, which is discussed at the end of this subchapter).

An example of the integration that will lead to the finite difference schemes will be given for the temperature equation, assuming that $\bar{u}_1^t$ and $\bar{u}_2^t$ are both positive. For the time derivative in equation 16, it is found that:

$$\int_0^{2\pi}\int_{\Delta z(i-\frac{1}{2})}^{\Delta z(i+\frac{1}{2})}\int_{\Delta r(j-\frac{1}{2})}^{\Delta r(j+\frac{1}{2})}\frac{dT}{dt}rdrdzd\phi = 2\pi j\Delta r^2\Delta z\frac{dT}{dt}$$

Note that $r = j\Delta r$ throughout the calculations. The other terms have been solved in the same way. A step-by-step derivation will be given for one convective term and one diffusive term from the temperature equation. For the convection term it is found that:

$$\int_0^{2\pi}\int_{\Delta z(i-\frac{1}{2})}^{\Delta z(i+\frac{1}{2})}\int_{\Delta r(j-\frac{1}{2})}^{\Delta r(j+\frac{1}{2})}\frac{d(uT)}{dz}rdrdzd\phi = 2\pi j\Delta r^2\int_{\Delta z(i-\frac{1}{2})}^{\Delta z(i+\frac{1}{2})}\frac{d(uT)}{dz}dz$$

It is allowed to take these terms out of the integral immediately, because they are not a function of the axial coordinate z. This expression simplifies as:

$$2\pi j\Delta r^2\int_{\Delta z(i-\frac{1}{2})}^{\Delta z(i+\frac{1}{2})}\frac{d(uT)}{dz}dz = 2\pi j\Delta r^2[uT]_{\Delta z(i-\frac{1}{2})}^{\Delta z(i+\frac{1}{2})}$$

The velocity at $\Delta z(i+1/2)$ is simply the average velocity between $\Delta z(i)$ and $\Delta z(i+1)$. The temperature is discretized according to the sign of $\bar{u}$. Assuming both $\bar{u}_1$ and $\bar{u}_2$, are positive, the following expression is then found:

$$2\pi j\Delta r^2[uT]_{\Delta z(i-\frac{1}{2})}^{\Delta z(i+\frac{1}{2})} = 2\pi j\Delta r^2\left[\left(\frac{u_{i+1,j}+u_{i,j}}{2}\right)T_{i,j} - \left(\frac{u_{i,j}+u_{i-1,j}}{2}\right)T_{i-1,j}\right]$$

This expression is now divided by the term in front of the time derivative to obtain the derivative in discretized form:

$$\frac{\partial(uT)}{\partial z} = \left[\left(\frac{u_{i+1,j}+u_{i,j}}{2\Delta z}\right)T_{i,j} - \left(\frac{u_{i,j}+u_{i-1,j}}{2\Delta z}\right)T_{i-1,j}\right] + \mathcal{O}(\Delta z)$$

For the radial diffusive temperature term, it is found that:

$$\int_0^{2\pi}\int_{\Delta z(i-\frac{1}{2})}^{\Delta z(i+\frac{1}{2})}\int_{\Delta r(j-\frac{1}{2})}^{\Delta r(j+\frac{1}{2})}\frac{1}{r}\frac{d}{dr}\left(r\frac{dT}{dr}\right)rdrdzd\phi = 2\pi\Delta z\int_{\Delta r(j-\frac{1}{2})}^{\Delta r(j+\frac{1}{2})}\frac{d}{dr}\left(r\frac{dT}{dr}\right)dr$$

Again, the derivatives drop, and one is left with:

$$2\pi\Delta z\int_{\Delta r(j-\frac{1}{2})}^{\Delta r(j+\frac{1}{2})}\frac{d}{dr}\left(r\frac{dT}{dr}\right)dr = 2\pi\Delta z\left[r\frac{dT}{dr}\right]_{\Delta r(j-\frac{1}{2})}^{\Delta r(j+\frac{1}{2})}$$

The expression on the right hand side is equal to:

$$2\pi\Delta z\left[r\frac{dT}{dr}\right]_{\Delta r(j-\frac{1}{2})}^{\Delta r(j+\frac{1}{2})} = 2\pi\Delta z\left(\Delta r(j+\frac{1}{2})\left(\frac{T_{i,j+1}-T_{i,j}}{\Delta r}\right) - \Delta r(j-\frac{1}{2})\left(\frac{T_{i,j}-T_{i,j-1}}{\Delta r}\right)\right)$$

This expression is divided by the terms in front of the time derivative to arrive at:

$$\frac{1}{r}\frac{\partial}{\partial r}\left(r\frac{\partial T}{\partial r}\right) = \left[\frac{(j+\frac{1}{2})T_{i,j+1} - 2jT_{i,j} + (j-\frac{1}{2})T_{i,j-1}}{j\Delta r^2}\right] + \mathcal{O}(\Delta r^2)$$

The time derivatives are approximated by a first order Euler forward method:

$$\frac{\partial f}{\partial t} = \frac{f_{i,j}^{t+1} - f_{i,j}^t}{\Delta t} + \mathcal{O}(\Delta t) \tag{38}$$

Parameter f can be both vorticity or temperature. The process of integrating terms over a small cylinder has been repeated for all terms inside the temperature-and vorticity equation to derive the difference schemes. When all average velocities are positive, for example, the following difference scheme is obtained for the temperature:

$$\frac{T_{i,j}^{t+1}-T_{i,j}^{t}}{\Delta t}+\frac{\bar{u}_1^t T_{i,j}^t-\bar{u}_2^t T_{i-1,j}^t}{\Delta z}+\frac{(j+\frac{1}{2})\bar{v}_1^t T_{i,j}^t-(j-\frac{1}{2})\bar{v}_2^t T_{i,j-1}^t}{j\Delta r}=\frac{T_{i+1,j}^t-2T_{i,j}^t+T_{i-1,j}^t}{\Delta z^2}+$$
$$\frac{(j+\frac{1}{2})T_{i,j+1}^t-2jT_{i,j}^t+(j-\frac{1}{2})T_{i,j-1}^t}{j\Delta r^2}+\epsilon\sigma$$

Similar equations are found for other signs of $\bar{u}_1$, $\bar{u}_2$, $\bar{v}_1$ and $\bar{v}_2$.

Special attention should be taken into account when dealing with the temperature equation at the center of the tank. Two terms contain $1/r$ which is undefined at $r=0$. The corresponding terms are the radial convective term and the radial diffusive term. To deal with the singularity at $r=0$, the two corresponding terms are rewritten. The radial convective term is rewritten as:

$$\frac{1}{r}\frac{\partial(rvT)}{\partial r}=v\frac{\partial T}{\partial r}+T\frac{\partial v}{\partial r}+\frac{vT}{r} \tag{39}$$

The symmetry boundary condition at the centerline ($\partial/\partial r=0$) enables us to write:

$$\frac{1}{r}\frac{\partial(rvT)}{\partial r}\bigg|_{r=0}=\frac{vT}{r} \tag{40}$$

The integration of this term at the centerline yields:

$$\int_0^{2\pi}\int_{\Delta z(i-\frac{1}{2})}^{\Delta z(i+\frac{1}{2})}\int_{-\frac{\Delta r}{2}}^{\frac{\Delta r}{2}}\frac{vT}{r}rdrdzd\phi=2\pi\Delta z\int_{-\frac{\Delta r}{2}}^{\frac{\Delta r}{2}}vTdr \tag{41}$$

When this integral is evaluated, one must use the symmetry of the system: $v_{i,-1}=v_{i,1}$ and $v_{i,0}=0$ to find the final discretized term for this expression:

$$\frac{1}{r}\frac{\partial(rvT)}{\partial r}\bigg|_{r=0}=\frac{2v_{i,1}T_{i,0}}{\Delta r}+\mathcal{O}(\Delta r) \tag{42}$$

The radial diffusive term where the other singularity will occur is also rewritten:

$$\left(\frac{1}{r}\frac{\partial}{\partial r}\left(r\frac{\partial T}{\partial r}\right)\right)=\frac{1}{r}\frac{\partial T}{\partial r}+\frac{\partial^2 T}{\partial r^2} \tag{43}$$

for the first term in equation 43, L'hôspitals rule has been applied:

$$\left(\frac{1}{r}\frac{\partial T}{\partial r}\right)_{r=0}=\frac{\partial^2 T}{\partial r^2} \tag{44}$$

Now the following form of equation 43 can be used at the center:

$$\left(\frac{1}{r}\frac{\partial}{\partial r}\left(r\frac{\partial T}{\partial r}\right)\right)_{r=0}=2\frac{\partial^2 T}{\partial r^2} \tag{45}$$

When this term is discretized, symmetry of the system has been used: $T_{i,-1}=T_{i,1}$. Then the discretized form of equation 43 at the center becomes:

$$\left(\frac{1}{r}\frac{\partial}{\partial r}\left(r\frac{\partial T}{\partial r}\right)\right)_{r=0}=4\left(\frac{T_{i,1}-T_{i,0}}{\Delta r^2}\right)+\mathcal{O}(\Delta r^2) \tag{46}$$

The remaining terms at the center are evaluated in the same manner as for the interior grid points, but the integral boundaries $-\Delta r/2$ and $\Delta r/2$ are used instead of $\Delta r(j-1/2)$ and $\Delta r(j+1/2)$.

5.1.4 Solving the Elliptic Equation

At each time-step, the new temperatures and vorticities are calculated at the interior nodes from the previous values. The temperatures at the boundaries are also calculated. The vorticity on the boundaries is evaluated later on in the process (as will be discussed later in the section).

The next step in the simulation is to solve the stream function equation. In order to do so, new values of the vorticity at the interior nodes are used. The stream function is integrated over a small cylinder and rewritten explicitly for the stream function Ψ:

$$\Psi_{i,j}^{s+1} = (1-\omega)\Psi_{i,j}^{s} + \frac{\omega\left(j\Omega_{i,j}^{s}\Delta r + \frac{1}{\Delta z^2}(\Psi_{i+1,j}^{s} + \Psi_{i-1,j}^{s+1}) + \frac{1}{\Delta r^2}\left(\frac{j}{j+\frac{1}{2}}\Psi_{i,j+1}^{s} + \frac{j}{j-\frac{1}{2}}\Psi_{i,j-1}^{s+1}\right)\right)}{\frac{2}{\Delta r^2} + \frac{1}{\Delta r^2}\left(\frac{j}{j-\frac{1}{2}} + \frac{j}{j+\frac{1}{2}}\right)} \tag{47}$$

This equation needs to be iterated to obtain a value for $\Psi_{i,j}$. A successive over relaxation (SOR) iteration has been used with ω as the accelerating parameter [24]. The value of this parameter is usually set between 1 and 2, and [24] uses a value of 1.9. For this research, some simulations are done to obtain the optimal value of ω, as will be discussed later. Subscript s represents the number of iterations. The iteration will stop when the following criterion is met:

$$\frac{|\Psi_{i,j}^{s+1} - \Psi_{i,j}^{s}|}{\max|\Psi_{i,j}^{s}|} \leq 1 \cdot 10^{-6} \tag{48}$$

5.1.5 Vorticity on the Boundaries

Now that the stream functions are obtained from the iteration, the next step in the simulation is to calculate the vorticity on the boundaries of the system. A Taylor expansion is used to get an explicit equation for the vorticity at the boundary in terms of the stream function. As an example, the derivation of the vorticity at the bottom ($z = 0$) will be given. At the other boundaries, comparable expressions are found. At the boundary at $z = 0$, Taylor expansions are made around $\Psi_{i,1}$ and $\Psi_{i,2}$ to get a second order expression for the wall vorticities.

$$\Psi_{1,j} = \Psi_{0,j} + \Delta z\frac{\partial\Psi}{\partial z} + \frac{\Delta z^2}{2}\frac{\partial^2\Psi}{\partial z^2} + \frac{\Delta z^3}{6}\frac{\partial^3\Psi}{\partial z^3} + ...$$

$$\Psi_{2,j} = \Psi_{0,j} + 2\Delta z\frac{\partial\Psi}{\partial z} + \frac{4\Delta z^2}{2}\frac{\partial^2\Psi}{\partial z^2} + \frac{8\Delta z^3}{6}\frac{\partial^3\Psi}{\partial z^3} + ...$$

Note that higher order terms have been left out of the equation. When using the boundary conditions for $z = 0$, $\Psi_{0,j} = 0$ and $\partial\Psi/\partial z = 0$, these terms cancel from the equations. If the third order term is isolated from the first equation, the following expression is found:

$$\frac{\partial^3\Psi}{\partial z^3} = \frac{6}{\Delta z^3}\left(\Psi_{1,j} - \frac{\Delta z^2}{2}\frac{\partial^2\Psi}{\partial z^2}\right)$$

This term is substituted to eliminate the third order term in the second equation:

$$\Psi_{2,j} = 8\Psi_{1,j} - 2\Delta z^2\frac{\partial^2\Psi}{\partial z^2}$$

After rewriting, the following expression is obtained:

$$\frac{\partial^2\Psi}{\partial z^2} = \frac{8\Psi_{1,j} - \Psi_{2,j}}{2\Delta z^2}$$

Using the definition of vorticity and the boundary conditions at $z = 0$, it is found that:

$$\Omega = -\frac{1}{r}\frac{\partial^2 \Psi}{\partial z^2}$$

If the expression of the second order derivative is substituted into the vorticity equation, one arrives at the final equation at $z = 0$:

$$\Omega_{0,j} = \frac{\Psi_{2,j} - 8\Psi_{1,j}}{2j\Delta r \Delta z^2} + \mathcal{O}(\Delta z^2) \tag{49}$$

The same method has been applied to the other boundaries. Note that $\Omega = 0$ at $r = 0$ for all z, so no equation is required for the vorticity at the axis of symmetry.

Next, the new values of the radial and axial velocity are calculated from the updated stream functions. A second order central difference scheme is used to calculate the velocities from the velocity equation. The following expressions are used:

$$u_{i,j} = \frac{\Psi_{i,j+1} - \Psi_{i,j-1}}{2j\Delta r^2} + \mathcal{O}(\Delta r^2) \tag{50}$$

$$v_{i,j} = -\frac{\Psi_{i+1,j} - \Psi_{i-1,j}}{2j\Delta r \Delta z} + \mathcal{O}(\Delta z^2) \tag{51}$$

For the axial velocity at $r = 0$, L'hôspitals rule has to be applied to avoid physical anomalies. A second order central difference scheme is used and combined with the axis of symmetry boundary condition to arrive at:

$$u_{i,1} = \frac{2\Psi_{i,2}}{\Delta r^2} + \mathcal{O}(\Delta r^2) \tag{52}$$

5.1.6 Discretization Method for PCM-Region

Now the equations inside the water region have been solved. Next, the system will compute the temperatures of the PCM region. First, the wall temperature must be calculated. In order to calculate the wall temperature, the interfacial boundary condition is discretized:

$$-k_w\left(\frac{T_{i,r_i} - T_{i,r_i-1}}{\Delta r}\right) = -k_s\left(\frac{T_{i,r_i+1} - T_{i,r_i}}{\Delta r}\right)$$

This expression can be rewritten to solve for the wall temperature:

$$T_{i,r_i} = \frac{k_w T_{i,r_i-1} + k_s T_{i,r_i+1}}{k_w + k_s}$$

Note that the dimensionless temperature of the water is converted to its dimensional form first. For the PCM region, only diffusive heat transfer is taken into account. The equations are similar the the temperature equation of water, but the nonlinear convective terms are absent. After discretizing it is found that:

$$H^{t+1}_{i,j^*} = H^t_{i,j^*} + \mathrm{Fo}_z\lambda(T_{i-1,j^*} - 2T_{i,j^*} + T_{i+1,j^*}) + \tag{53}$$

$$\frac{\mathrm{Fo}_r\lambda}{j^*}\left((j^* + 1/2)T_{i,j^*+1} - 2j^*T_{i,j^*} + (j^* - 1/2)T_{i,j^*-1}\right) + \mathcal{O}(\Delta r^2) + \mathcal{O}(\Delta z^2) + \mathcal{O}(\Delta t) \tag{54}$$

In these equations $j^* = j + n_r$ and λ is a conversion term to convert the temperatures inside the equation to specific enthalpies:

$$\lambda = \frac{k_s}{\rho_s \alpha_s}$$

Furthermore, two different Fourier numbers are found:

$$\mathrm{Fo}_z = \frac{\alpha_s \Delta t}{\Delta z^2} \quad \mathrm{Fo}_r = \frac{\alpha_s \Delta t}{\Delta r^2}$$

The Fourier numbers are dimensionless parameters defining the ratio of the rate of thermal diffusion to thermal energy storage. Notice that at $j^* = 1$, the term T_{i,j^*-1} will be equal to the wall temperature. The values of the specific enthalpies are then converted to temperatures using the explicit enthalpy method. This conversion is straightforward and will not be shown.

Now the wall temperature and all interior temperatures of the PCM region are known, and the temperatures at the boundaries of the PCM region are evaluated using the suitable boundary conditions.

5.1.7 Critical Time-Step

The final step in the simulation is to find the value of the critical time-step Δt_{cr}. Time-steps larger than this time-step may cause severe instabilities in the solution. After each iteration a new critical time-step is calculated, and a fraction of this time-step will be used as time-step in the next iteration to ensure stability of the solution. The most stringent equations with respect to the size of the maximum allowable time-step are the temperature equations for water (at the interior and at $r = 0$) and the vorticity equation. The diffusive heat transfer equations for the PCM have been disregarded because they are less stringent on the critical time step. To find the size of Δt_{cr}, a Von Neumann stability analysis has been applied on the equations [23]. The three equations need to be rewritten into a form such that all constants regarding $T_{i,j}$ or $\Omega_{i,j}$ are collected and put together. The sum of these constants must be greater or equal than 0 to preserve stability. As an example, the equation for temperature will be shown in the case that all average temperatures $\bar{u}$ and $\bar{v}$ will be positive. The equation of temperature is then given by:

$$T_{i,j}^{t+1} = T_{i,j}^{t}\left(1 - \frac{\bar{u}_1 \Delta t}{\Delta z} - (j + 1/2)\frac{\bar{v}_1 \Delta t}{\Delta r} - \frac{2\Delta t}{\Delta z^2} - \frac{2\Delta t}{\Delta r^2}\right) + ...$$

The remainder of the equation is not important, since it only contains constants regarding temperatures of neighbouring nodes. The term between brackets should be greater or equal to 0 according to [24] to preserve stability:

$$\left(1 - \frac{\bar{u}_1 \Delta t}{\Delta z} - (j + 1/2)\frac{\bar{v}_1 \Delta t}{\Delta r} - \frac{2\Delta t}{\Delta z^2} - \frac{2\Delta t}{\Delta r^2}\right) \geq 0$$

From this equation the critical value of the time-step can be evaluated:

$$\Delta t_{cr}(1) \leq \left(\frac{\bar{u}_1}{\Delta z} + (j + 1/2)\frac{\bar{v}_1}{\Delta r} + \frac{2}{\Delta z^2} + \frac{2}{\Delta r^2}\right)^{-1} \tag{55}$$

The same derivation has been done for the temperature equation at $r = 0$ and the vorticity equation. Note that these expressions change when the sign of the average velocities $\bar{u}$ and $\bar{v}$ change. The time-step that will be used in the next iteration should be less than the critical value to be sure that stability is preserved. To reduce computational time, [24] uses 95% of the critical time step as the new time-step. However, since the truncation error of the time derivative is relatively large ($\mathcal{O}(\Delta t)$), also smaller constant time-steps are tested in this report. However, the default setting throughout this report will be 95%:

$$\Delta t = 0.95 \cdot \min(\Delta t_{cr}(1), \Delta t_{cr}(2), \Delta t_{cr}(3)) \tag{56}$$

Note that three values of the critical time-step are calculated: one for the equation for temperature, one for the equation for temperature at $r = 0$ and one for the vorticity equation, $\Delta t_{cr}(1)$,$\Delta t_{cr}(2)$ and $\Delta t_{cr}(3)$ respectively. The total simulation time is then updated using $t^{\text{new}} = t^{\text{old}} + \Delta t$.

Now all parameters have been calculated and the iteration is repeated until the time t is equal to the total simulation time t_{sim}. When the system leaves the iterations, plots are generated for parameters such as stream function and temperature. These parameters correspond to the time t_{sim} at which the simulation stops.

5.1.8 Heater

Finally, the modeling of the heater will be explained. The actual heater provides $Q = 2.0$ kW of heat and has a complex geometry. For simplicity, it is modeled to be a cylinder with radius 4.25 mm and a height of 15.0 cm. These values lead to a volumetric heating value of $q = 2.34 \cdot 10^8$ W/m^3. This value has been used in the simulations and has been held constant. If, for example, $\Delta r = 1$ cm, the volume of the heater in the simulation has been calculated and the value of Q has been changed so that q remains fixed. The higher the number of nodes, the closer Q gets to 2.0 kW. The motivation to do so is due to the fact that if q is not held constant, no proper comparisons can be made when the number of nodes are changed.

For the charging model without PCM (the conventional hot water tank), the volume that was occupied by the PCM is now occupied by the same volume of water. A fair comparison regarding the storage capacity between the two models can now be made since their total volume is the same. The inter-facial boundary condition is replaced by a perfectly isolated surface at $r = r_o$. The other boundary conditions remain the same.

5.2 Discharging Model

To simulate the in- and out flow of water (discharging the tank), another model has been set up. The method of solving the equations is very similar to the charging mode. However, different dimensionless parameters characterize the flow [25]. Since the conservative forms of the equations turned out to oscillate around $r = 0$, the non-conservative formulation of the governing equations has been used [23]. Also, the boundaries for the stream function and the vorticity change due to the in- and outflow of water.

The geometry of the system is the same as for the charging model, but between $r = 0$ and $r = r_{\text{jet}}$ an opening is present at $z = 0$ and $z = h$, allowing water to flow in- and out of the system. Cold water (T_o) flows in at $z = 0$ and hot water (T_h) leaves at $z = h$, see figure 6. Both openings at the top and bottom have the same size.

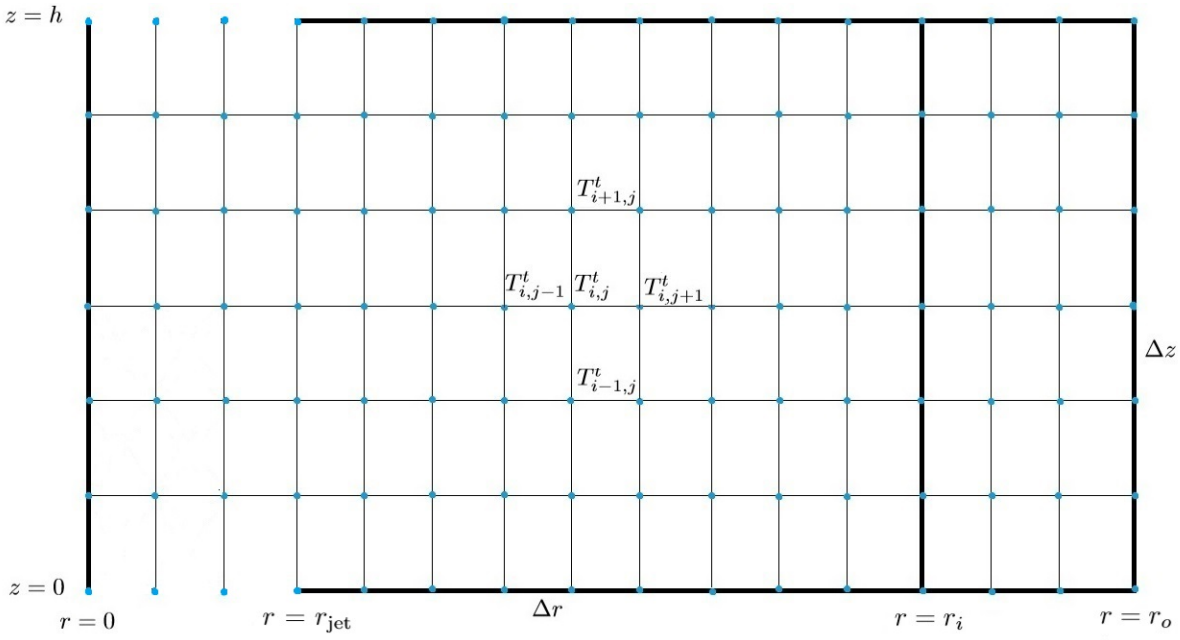

Figure 6: *System geometry for simulating the discharging cycle. Note that the scales are not representative: the jet opening is only a small fraction of the diameter of the tank.*

5.2.1 Governing Equations

Another set of dimensionless parameters is introduced to solve the governing equations for the discharge cycle. They are the following [25]:

$$t = \frac{u_{\text{jet}}}{h}t^* \quad z = \frac{z^*}{h} \quad r = \frac{r^*}{h} \quad v = \frac{v^*}{u_{\text{jet}}} \quad u = \frac{u^*}{u_{\text{jet}}} \quad T = \frac{T^* - T_h}{T_o - T_h} \tag{57}$$

The jet velocity u_{jet} is used as a characteristic velocity and is calculated by:

$$u_{\text{jet}} = \frac{Q_v}{\pi r_{\text{jet}}^2} \tag{58}$$

The term Q_v represents the volumetric flow rate at the inlet of the tank, which is known.

Unlike the charging model, a non-conservative form of the governing equations will be used. To convert the conservative formulation into a non-conservative formulation, a modified vorticity is introduced [23]:

$$\Omega' = \frac{1}{r}\Omega \tag{59}$$

This expression is substituted into the conservative stream function- and vorticity equation. Next, the product rule is used to work out all derivatives. The velocity field is now assumed to be divergent free, so:

$$\Omega'(\vec{\nabla} \cdot \vec{u}) = T(\vec{\nabla} \cdot \vec{u}) = \vec{0} \tag{60}$$

These expressions are used to cancel some derivative terms in the vorticity-and temperature equations. After canceling terms and substituting the dimensionless parameters, the following governing equations arise:

$$v = -\frac{1}{r}\frac{\partial \Psi}{\partial z} \quad u = \frac{1}{r}\frac{\partial \Psi}{\partial r} \tag{61}$$

$$\frac{1}{r}\frac{\partial^2 \Psi}{\partial z^2} + \frac{\partial}{\partial r}\left(\frac{1}{r}\frac{\partial \Psi}{\partial r}\right) = -\Omega' r \tag{62}$$

$$\frac{\partial T}{\partial t} + u\frac{\partial T}{\partial z} + v\frac{\partial T}{\partial r} = \frac{1}{\text{Pe}}\left[\frac{\partial^2 T}{\partial z^2} + \frac{1}{r}\frac{\partial}{\partial r}\left(r\frac{\partial T}{\partial r}\right)\right] \tag{63}$$

$$\frac{\partial \Omega'}{\partial t} + u\frac{\partial \Omega'}{\partial z} + v\frac{\partial \Omega'}{\partial r} = \frac{-\text{Ri}}{r}\frac{\partial T}{\partial r} + \frac{1}{\text{Re}}\left[\frac{\partial^2 \Omega'}{\partial z^2} + \frac{1}{r}\frac{\partial}{\partial r}\left(\frac{1}{r}\frac{\partial (r^2 \Omega')}{\partial r}\right)\right] \tag{64}$$

The flow is characterized by the Peclet number, Richardson number and the Reynolds number respectively:

$$\text{Pe} = \frac{u_{\text{jet}} h}{\alpha} \quad \text{Re} = \frac{u_{\text{jet}} h}{\nu} \quad \text{Ri} = \frac{\text{Gr}}{\text{Re}^2} = \frac{g\beta(T_o - T_h)h}{u_{\text{jet}}^2} \tag{65}$$

The Peclet number is the ratio of convective heat transport over diffusive heat transport. The Reynolds number is the ratio of inertial forces over viscous forces. Finally, the Richardson number is the ratio of natural convection and forced convection. For the derivation of the buoyancy source term, the reader is referred to appendix C.

The governing equations for the PCM remain the same as for the charging model. Instead of solid PCM to start with, liquid PCM is present which will follow from the initial condition.

5.2.2 Boundary- and Initial Conditions

At the inlet, it is assumed that there is no radial flow and the axial flow has a parabolic profile in the following form:

$$u(r) = 1 - \left(\frac{r}{r_{\text{jet}}}\right)^2 \tag{66}$$

Note that a factor u is missing in front of this equation, but since this term is equal to 1.0 from nondimensionalizing, it is left out. The maximum velocity is now defined at $r = 0$ and the minimum velocity is defined at $r = r_{\text{jet}}$. Since $v = 0$ at the inlet, the stream function at the inlet can be calculated according to:

$$\Psi = \int_0^r u(r) r dr = \frac{r^2}{2}\left(1 - \frac{1}{2}\left(\frac{r}{r_{\text{jet}}}\right)^2\right) + c = \Psi_{\text{in}}(r) \tag{67}$$

The integration constant c is set to 0, since the stream function is 0 at $r = 0$. For brevity, the stream function at the inlet is called $\Psi_{\text{in}}(r)$. The boundary conditions for the system are now the following:

$$\Psi = \frac{\partial u}{\partial r} = v = \frac{\partial T}{\partial r} = 0 \quad r = 0 \quad 0 \leq z \leq 1 \tag{68}$$

$$T = T_s \quad -k\frac{\partial T}{\partial r} = -k_s \frac{\partial T_s}{\partial r} \quad \frac{\partial \Psi}{\partial r} = 0 \quad \Psi = \Psi_{\text{in}}(r_{\text{jet}}) \quad r = r_i \quad 0 \leq z \leq 1 \tag{69}$$

$$\frac{\partial T_s}{\partial r} = 0 \quad r^* = r_o^* \quad 0 \leq z^* \leq h \tag{70}$$

$$\frac{\partial \Psi}{\partial z} = 0 \quad \Psi = \Psi_{\text{in}}(r_{\text{jet}}) \quad \frac{\partial T}{\partial z} = 0 \quad z = 1 \quad r_{\text{jet}} \leq r \leq r_i \tag{71}$$

$$\frac{\partial T_s}{\partial z} = 0 \quad z^* = h \quad r_i^* \leq r^* \leq r_o^* \tag{72}$$

$$\frac{\partial \Psi}{\partial z} = 0 \quad \Psi = \Psi_{\text{in}}(r_{\text{jet}}) \quad \frac{\partial T}{\partial z} = 0 \quad z = 0 \quad r_{\text{jet}} \leq r \leq r_i \tag{73}$$

$$\frac{\partial T_s}{\partial z} = 0 \quad z^* = 0 \quad r_i^* \leq r^* \leq r_o^* \tag{74}$$

$$T = 1 \quad \Psi = \Psi_{\text{in}}(r) \quad \frac{\partial \Psi}{\partial z} = 0 \quad 0 \leq r \leq r_{\text{jet}} \quad z = 0 \tag{75}$$

$$T = T^- \quad \Psi = \Psi_{\text{in}}(r) \quad \frac{\partial \Psi}{\partial z} = 0 \quad 0 \leq r \leq r_{\text{jet}} \quad z = 1 \tag{76}$$

With the introduction of the in-and outlet of the tank, the boundary conditions change significantly. First of all, at the centerline Ω may be 0, but Ω' may not be 0 [23]. For Ω' at the centerline, the following equation is used:

$$\frac{\partial \Omega'}{\partial t} + u\frac{\partial \Omega'}{\partial z} = -\text{Ri}\frac{\partial^2 T}{\partial r^2} + \frac{1}{\text{Re}}\left[\frac{\partial^2 \Omega'}{\partial z^2} + 4\frac{\partial^2 \Omega}{\partial r^2}\right] \tag{77}$$

The temperature at the outlet has simply set to the same temperature of their neighbouring nodes at a distance Δz lower. The initial conditions are the following:

$$\Psi = \Omega' = 0 \quad T = 0 \quad t = 0 \quad 0 \leq z \leq 1 \quad 0 \leq r \leq r_i \tag{78}$$

$$T_s = T_h \quad t = 0 \quad 0 \leq z^* \leq h \quad r_i^* \leq r^* \leq r_o^* \tag{79}$$

5.2.3 Discretization Method for Water Region

The governing equations are integrated over a small cylinder, as has been done and showed at the charging model section. The convection terms are discretized using a second order upwind scheme, defined as:

$$\left(u\frac{\partial f}{\partial z}\right)_{i,j} = u_{i,j}\left(\frac{3f_{i,j} - 4f_{i-1,j} + f_{i-2,j}}{2\Delta z}\right) + \mathcal{O}(\Delta z^2) \quad u_{i,j} > 0 \tag{80}$$

$$\left(u\frac{\partial f}{\partial z}\right)_{i,j} = u_{i,j}\left(\frac{-3f_{i,j} + 4f_{i+1,j} - f_{i+2,j}}{2\Delta z}\right) + \mathcal{O}(\Delta z^2) \quad u_{i,j} < 0 \tag{81}$$

The term f can both be temperature or the modified vorticity. The same scheme holds for the radial counterparts involving $v_{i,j}$. The convection terms are now defined everywhere except for the nodes adjacent to the boundaries. For those nodes only a first order upwind scheme is used.

5.2.4 Solving the Elliptic Equation

The stream function equation is solved by the SOR iteration but the vorticity Ω is replaced by $r\Omega'$. The solving procedure remains the same as for the charging model, but a larger error was allowed for stopping the SOR iteration:

$$\frac{|\Psi_{i,j}^{s+1} - \Psi_{i,j}^{s}|}{\max|\Psi_{i,j}^{s}|} \leq 1 \cdot 10^{-3} \tag{82}$$

Using a smaller error lead to very high computational times while the results were comparable to the results with a larger error. Therefore a larger error was allowed for both discharging models.

5.2.5 Vorticity on the Boundaries

The modified vorticity at the inlet can be evaluated using an analytical expression. Since the velocity profile is known, and there is no radial velocity component, one can write:

$$\Omega' r = -\frac{du}{dr} \tag{83}$$

So that the modified vorticity is equal to

$$\Omega' = \frac{2}{r_{\text{jet}}^2} \tag{84}$$

At the outlet, the same parabolic velocity profile is used as for the inlet for the axial velocity. However, there may also be a non-zero radial velocity component which has been discretized using:

$$v = -\frac{1}{r}\frac{\partial \Psi}{\partial z} = -\frac{1}{j\Delta r}\left(\frac{\Psi_{Nz,j} - \Psi_{Nz-1,j}}{\Delta z}\right) + \mathcal{O}(\Delta z) \tag{85}$$

This equation is valid for the region $\Delta r \leq r \leq r_{\text{jet}}$. At the centerline, the radial velocity is 0. The discretization for v in the jet region is first order accurate, but all the required nodes are in the physical domain. Finally, it is assumed that there is no axial gradient in vorticity at the outlet:

$$\frac{\partial \Omega'}{\partial z} = 0 \tag{86}$$

For the solid wall parts, the procedure has been repeated from the charging method, using Taylor expansions. However, instead of a second order approximation, now a first order approximation has been used. First order approximations for the wall vorticity are less susceptible to instabilities at high Reynolds numbers. To get the expression of the modified vorticity at the wall instead of vorticity, all these terms are multiplied by $1/r$.

5.2.6 Critical Time-Step

The critical time-step is calculated using the Von Neumann stability analysis (the same procedure as has been described for the charging model). The complete iteration is repeated until an outlet temperature of T_c is obtained.

5.3 Temporal and Spatial Convergence Tests

In this subsection, the methods will be presented regarding the determination of temporal and spatial convergence. A temporal convergence test was executed first. A simulation was run for $t = 15$ minutes, since this will be the first moment the results will be shown. The default setting of taking 95% of the critical time-step was changed to a smaller fixed time-step and results for the maximum stream function and maximum vorticity were compared. Simulations were done on a coarse grid ($(n_z, n_r) = (36, 24)$) to minimize the CPU-time required for each simulation. The same method has been applied to the PCM-enhanced tank model.

Next, a spatial convergence test was performed. Three mesh sizes have been tested and the grid convergence index has been evaluated according to [31]. The coarse grid consists of 36 x 24 nodes (36 axial-and 24 radial nodes) while the medium sized grid consists of 36 x 54 nodes and the fine grid consists of 54 x 81 nodes. The nodes are chosen such that $\Delta r = \Delta z$ and the ratio of refinement is 1.5. The dimensions of the axial and radial segments are not equal for both models, since r_o =20 cm for the conventional hot water tank while r_i=15 cm for the PCM-enhanced hot water tank. The rate of convergence has been evaluated by using the grid convergence index (GCI). Different simulation times were used since the problem is assumed to be transient. To perform the spatial convergence test, the maximum values of the stream function and vorticity have been obtained. The method to perform the spatial convergence test is described below. For numerical values regarding the CPU-times, the values of the maximum stream function and vorticity and the results from the spatial grid depency test, the reader is referred to tables **??**, 8 and 9 in appendix A respectively.

To evaluate the grid convergence index, the order of convergence p is calculated first, using

$$p = \ln\left(\frac{\Psi_{\text{coarse}} - \Psi_{\text{medium}}}{\Psi_{\text{medium}} - \Psi_{\text{fine}}}\right) \Big/ \ln(1.5) \tag{87}$$

The term ln(1.5) comes from the ratio of refinement, which in our case is 1.5. The grid convergence index can now be evaluated using:

$$\text{GCI} = \frac{F_s |err|}{1.5^p - 1} \tag{88}$$

The error between two different grid types is denoted by err. Two GCI values have been calculated: one for the difference medium-coarse and one for the difference fine-medium. The term F_s represents a safety factor which is 1.25 when using three different grid types. Finally, a check has been performed to see whether results fall within the asymptotic range of convergence (ARC):

$$\text{ARC} = \frac{\text{GCI}_{2,3}}{1.5^p \cdot \text{GCI}_{1,2}} \tag{89}$$

The value of ARC should be close to 1, to fall within the range of convergence.

A Richardson extrapolation is performed to estimate true values in the limit of zero grid spacing. For the stream function this limit is calculated using

$$\Psi_{\text{true}} = \Psi_{\text{fine}} + \left(\frac{\Psi_{\text{fine}} - \Psi_{\text{medium}}}{1.5^p - 1}\right) \tag{90}$$

This exact same procedure is applied to the vorticity as well. The same equations are used but the stream function is then replaced by the vorticity.

For the discharge model the outlet temperatures will be plotted for different mesh sizes since the parameter of interest is the outlet temperature. The same method was applied by [25].

6 Results

In this section the results for both models will be presented. Section 6.1 will present results for the charging model for both tanks and section 6.2 will present results for the discharging model for both tanks.

6.1 Results for charging model

The properties that were used to perform the simulations for the charging model are presented in table 4. The value of q has been calculated according to the algorithm that was implemented into MATLAB. All thermal properties of water were evaluated at the average temperature of T_o and T_h.

Parameter	Value
h	30 cm
r_i	15 cm
r_o	20 cm
T_o	20°C
T_h	70°C
Pr	6.5
Gr	$5.4{\cdot}10^9$
q	$2.34{\cdot}10^8$ W/m^3
ω	1.8

Table 4: *Tank dimensions and other parameters used in the charging model. Note that for the cases without PCM, r_i is not taking place in the calculations.*

The results of the temporal convergence test are shown in table 5. It can be seen that the relative error for the stream function between the smallest time-step and the default setting is approximately 11.8%. The relative error for the stream function between the smallest time-step and the intermediate time-step is 0.5%. The errors for the vorticity are negligible. Since simulations were performed using the coarsest grid, and the final simulation should run for at least one hour, the option of using the smallest and intermediate time-steps have been disregarded. Those small time steps would cause impractical CPU times when using the fine grid.

To complete the spatial convergence test, more and longer simulation times are required. The same method would then be applied using small time-steps and the default setting. However, since the simulation times are very long (up to 9 hours), the assumption has been made that the overall temporal error doesn't change much during the simulation and will maintain around 10-15%. It would be too time consuming to perform such tests for all required simulation times.

Time-step Δt [s]	$\Psi_{\max}$ [m^3/s]	$\Omega_{\max}$ [Hz]	CPU
$1 \cdot 10^{-4}$	$7.56{\cdot}10^{-5}$	15.59	3.9 hrs.
$1 \cdot 10^{-3}$	$7.52{\cdot}10^{-5}$	15.67	22.9 min.
$0.95 \cdot \Delta t_{\text{cr}}$	$8.45{\cdot}10^{-5}$	15.60	2.3 min.

Table 5: *Results of the temporal convergence test for the conventional hot water tank. A coarse grid was used (36x24) and the properties were evaluated at $t = 15$ minutes in all cases.*

The same method has been applied to the PCM-enhanced tank model. The results for this model are shown in table 6. The relative error for the stream function between the smallest time-step and the default setting is 14.3%. For the vorticity, the relative error was negligible. The required CPU-time of the default setting is approximately 93 times faster than for the smallest time step. Since the charging model with PCM should run for 9 hours and taking into account that the mesh refinement will even increase the computational times more, the default setting has been used.

Time-step Δt [s]	$\Psi_{\max}$ [m^3/s]	$\Omega_{\max}$ [Hz]	CPU
$1 \cdot 10^{-4}$	$5.19 \cdot 10^{-5}$	18.43	3.9 hours.
$1 \cdot 10^{-3}$	$6.09 \cdot 10^{-5}$	18.51	26.5 min.
$0.95 \cdot \Delta t_{\text{cr}}$	$5.93 \cdot 10^{-5}$	18.28	2.5 min.

Table 6: *Results of the temporal convergence test for the PCM-enhanced hot water tank. A coarse grid was used (36x24) and the properties were evaluated at $t = 15$ minutes in all cases.*

The CPU time required to simulate 60 minutes for the conventional hot water tank were the following: 7.1 minutes, 1.0 hours and 7.2 hours for the coarse, medium and finest grid respectively. To simulate 9 hours for the PCM-enhanced hot water tank, the CPU times were 46.3 minutes, 4.7 hours and 31.9 hours for the coarse, medium and finest grid respectively.

For the spatial convergence test, plots have been generated indicating the maximum values of the stream function for each simulation. The results are shown in figure 7.

As can be seen from figure 7, the stream functions for both models are converging, but they are outside the asymptotic range of convergence. The ARC values for the stream functions lie within 0.34 and 0.66 while they should be approximately 1.0 for convergence to be reached (see table 9 in appendix A). Since results are not close to the asymptotic range of convergence, the Richardson extrapolation has not been applied, since its validity would be questionable.

The order of convergence, p, should be close to 1.0 since the model is first order accurate in a mathematical point of view. However, as stated by Torrance et al. [32], the order of convergence tends to a second order system. Values near $p = 2.0$ are expected for this model. The reason is the use of the conservative form of the equations. Vorticity and energy are conserved in such a model, while for the non-conservative form this is not the case [32]. It can indeed be seen that the rate of convergence for the stream function is closer to 2.0 than to 1.0 (see table 9 in appendix A), although large deviations are seen. This is another indication that the grid size is not fine enough for an accurate approximation of the governing equations.

The reason for not reaching the asymptotic range of convergence is numerical (or false) diffusivity within the system. Numerical diffusivity is introduced by discretizing the nonlinear convection terms and this phenomenon is worse for coarser grids. The cell Peclet number is used as an indicator of the ratio numerical diffusivity over physical diffusivity and is defined as follows:

$$\text{Pe}_{\text{cell}} = \frac{\alpha_{\text{num}}}{\alpha} = \frac{u \Delta z}{\alpha} \tag{91}$$

For the radial velocity, a similar equation is used, but with $v\Delta r$ as the numerical diffusivity. From our simulations, cell Peclet numbers of $\mathcal{O}(10^1)$ are found at the interior grid points for the finest mesh (after 5 minutes). Near the center, cell Peclet numbers of $\mathcal{O}(10^4)$ are present in the finest mesh (after 5 minutes). From these values, it can be concluded that numerical diffusivity is dominant over the physical diffusivity. The simulations show more 'smeared out' solutions than the actual solution. Since this is the case, the results are shown in appendix B instead of in this section.

However, the overall behaviour is as expected. Hot water rises at the center and hits the top of the tank. A stagnation point is formed at the top center and from there the hot fluid is spread radially outwards until it hits the right wall. Depending on the wall- and fluid temperature, the fluid will move downwards under the influence of the inertial forces to the point where inertial forces and the opposing buoyancy forces are in equilibrium. The fluid will then move towards the center of the tank where it is entrained by the jet at the centerline.

Although the overall behaviour of the system is as expected, no hard conclusions can be drawn from the system due to the amount of numerical diffusion. However, several general conclusions can be drawn from the overall behaviour. First of all, since the tank will be stratified in some way, the melting process will be slowest at the bottom of the tank at the outer edges. To melt the PCM that is located here, the longest time is required. This can also be seen from the figures in appendix B. After 9 hours, the PCM at the right lower corners is still solid. Secondly, it can be concluded that when RT Rubitherm is used as PCM, melting is a

very slow process in this configuration. One could conclude that, based on diffusion only, 5 cm PCM is an impractical thickness to fully melt. It takes a long time and it does not even increase the energy capacity of the tank when using 5.0 cm. Using less PCM or a lower value of latent heat could increase the total melting time for this process, but then the energy capacity is decreased rather than increased. Another solution could be to lower the melting temperature so that more heat is transferred to the PCM while charging. This will reduce the performance of the discharging cycle. In reality, heat transfer in the PCM also takes place via convection when melting, which is ignored in this research paper. Convection will increase the melting rate, so future models should incorporate convection as well to investigate the extend to which the melting rate is increased.

Finally, some suggestions are made regarding the discretization scheme of the nonlinear convection terms. A special form of a first order upwind scheme was used to model this process for two main reasons. First of all, since the cell Peclet number is very high, higher order accurate schemes such as QUICK are less stable [33]. Nonlinear schemes such as van Leer are stable but they neglect the inclination of the flow direction [33]. Secondly, the method that was used in this paper solved the conservative form of the governing equations which conserved energy and vorticity. The major drawback of a first order system is the large amount of numerical diffusivity. One solution to reduce the amount of numerical diffusivity would be to follow the streamlines to take into account flow direction [33]. Three models are proposed by [33] that may be used as a substitute for the convection terms in the current model: the CUPID-scheme (Corner UPwInD), the SUCCA-scheme (Skew Upwind Corner Convection Algorithm) and the SUPER-scheme (Skew UPwind and cornER algorithm) [33].

Instead of changing the discretization method of the nonlinear convection terms, the grid could also be refined at some critical positions inside the tank, while the remainder of the grid remains coarse. For example, one could use a very fine grid at $r = 0$ and the other three boundaries, while keeping the remainder of the grid coarse. Since most numerical diffusion will occur at an inclined flow direction with respect to the grid direction, a very fine grid could be used at other places where this effect is present (for example at the corners of the tank).

Finally, another solution would be to refine the grid nonetheless, but use a different program to execute the simulations. There are programs available specially designed for numerical computations such as FORTRAN, which may be quicker than MATLAB. A Program like ANSYS FLUENT, which is based on finite volume methods, is another alternative program which could be used.

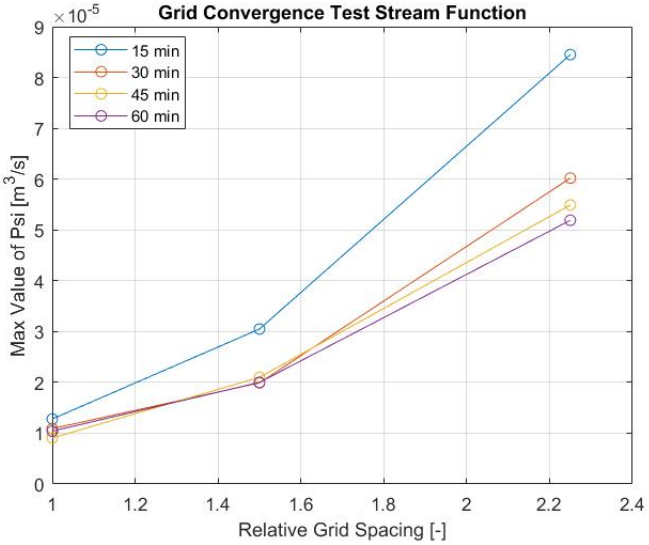

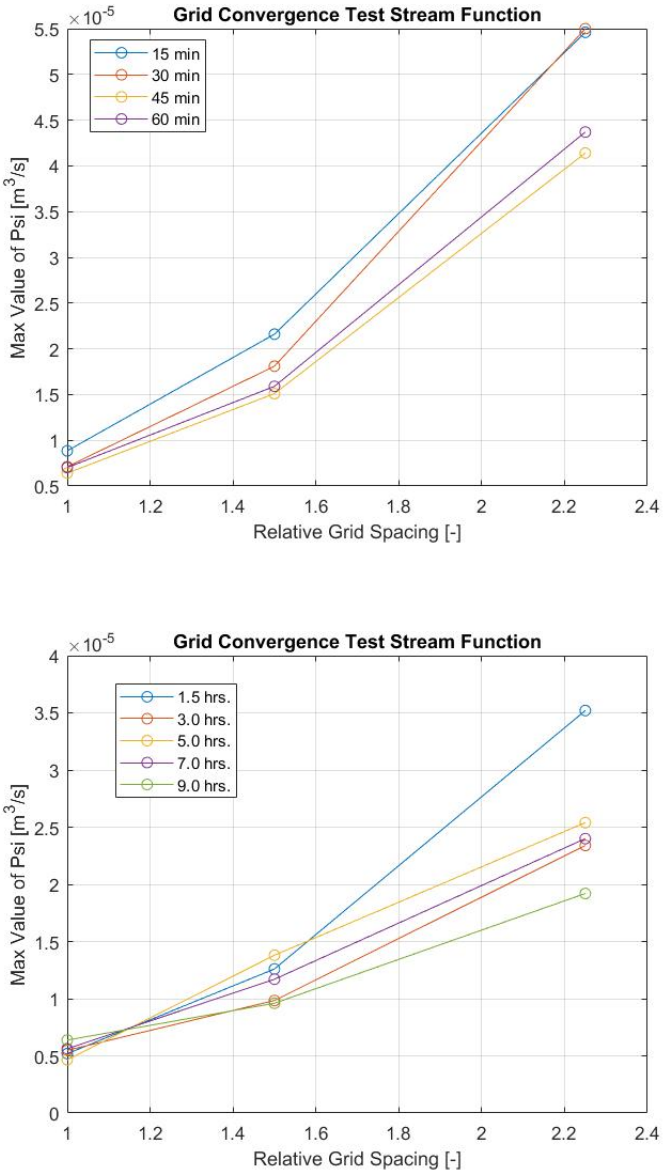

Figure 7: *Results of the spatial convergence test. At the top, maximum values for the stream function are shown for the conventional hot water tank. The middle and bottom figures show these results for the PCM-enhanced hot water tank.*

6.2 Results for discharging model

The constant properties during the discharging simulations for the conventional and PCM-enhanced hot water tank are shown in table 7. The conventional hot water tank contains more water volume than the PCM-enhanced hot water tank. For honest comparison, the volumetric flow rate has been adapted, so the expected discharge time for both tanks is the same.

Parameter	Conventional HWT	PCM-enhanced HWT
h	30 cm	30 cm
r_i	-	15 cm
r_o	20 cm	20 cm
T_o	20 °C	20 °C
T_h	70 °C	70 °C
Pe	$8.15{\cdot}10^5$	$4.16{\cdot}10^5$
Re	$1.25{\cdot}10^5$	$6.39{\cdot}10^4$
Ri	0.35	1.33
u_{jet}	0.42 m/s	0.21 m/s
Q_v	3.0 L/min	1.69 L/min
ω	1.3	1.3

Table 7: *Constants used in the simulations for the conventional and PCM-enhanced hot water tanks. These constants were evaluated at the finest grid.*

For the temporal convergence test, the coarsest grid was used (108x72) and the outlet temperature has been plotted as function of time. Both the default time step (changing every iteration) as well as a smaller constant time step was used to compare the results. The magnitude of the constant time step was defined as $\Delta t = 1 \cdot 10^{-4}$. The results are shown in figure 8. It can be seen that using smaller time steps does not cause big differences in the outlet temperature. The CPU of simulations using smaller time steps was 12.8 hours for the conventional hot water tank and 14.3 hours for the PCM-enhanced hot water tank. Approximately 30 minutes were required for both models using the default time step. To save computational time, the default time step has been chosen in the remainder of this research paper.

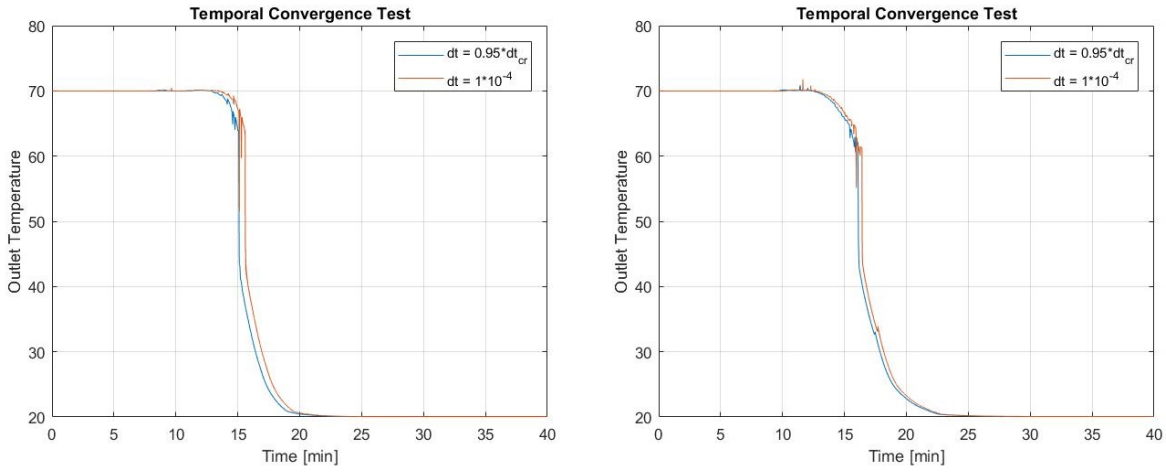

Figure 8: *Temperoral convergence tests for the conventional hot water tank (left) and the PCM-enhanced hot water tank (right).*

The spatial convergence tests are performed in the same manner as the temporal convergence tests. Since

the outlet consists of multiple nodes, having different temperatures, one node has been chosen to simulate the outlet temperature. This node is located a distance Δr from the center: $(z, r) = (h, \Delta r)$. The reason to do so is to exclude the center of tank, which is treated slightly different than its neighbouring nodes to avoid the singularity at $r = 0$. The results are shown in figure 9.

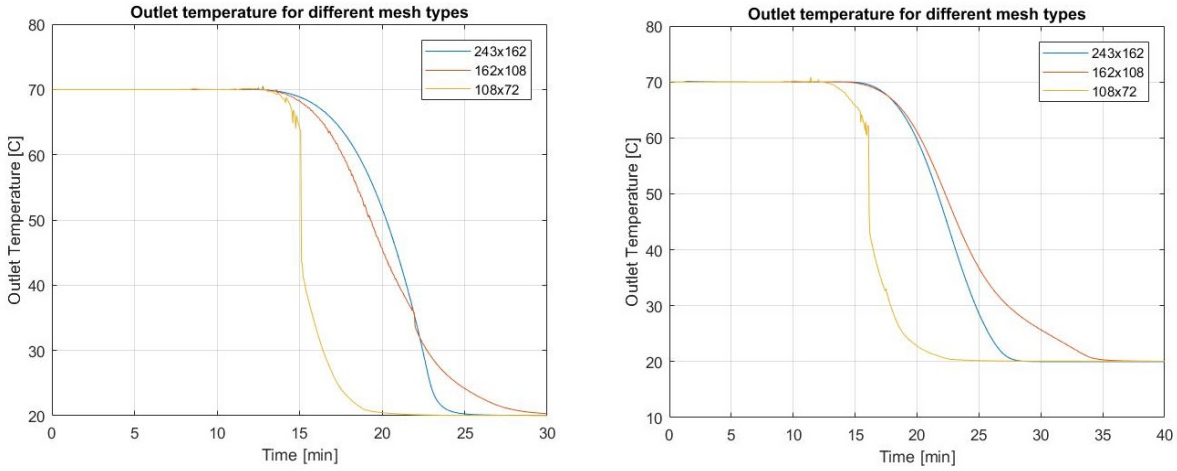

Figure 9: *Spatial convergence test for the conventional hot water tank (left) and for the PCM-enhanced hot water tank (right). In the discharge cycle, 108x72 is the coarsest grid.*

As can be seen from figure 9, the coarsest grid shows completely different results than the other two grids for both models. Using the coarsest grid lead to axial velocities which were higher than the inlet jet velocity at $r = 0$ for all z. This resulted in a quicker discharging cycle for both models. Values between u_{jet} and $2u_{\text{jet}}$ were seen. As the grid was refined, these velocities reduced except for the axial velocities at $r = 0$ very close to the inlet jet. To solve this problem, the grid should be refined more or smaller time steps should be used. However, to reduce computational effort, these nonphysical velocities over a small range of nodes were not improved. The difference between the medium sized mesh and the fine mesh was caused by numerical diffusion. A finer mesh lead to less numerical diffusion so that the moving thermocline is less spread out. The outlet temperature will therefore have a steeper decline as can be seen from figure 9.

The finest grid has been used to predict the results as accurate as possible. Further refinements of the mesh should be taken into account, but this would result in very high computational times. The author of this paper assumed that using a 243x162 is fine enough for conclusions to be drawn.

Temperature contours of both systems are generated every 5 minutes in the simulation and the results are shown in figure 10.

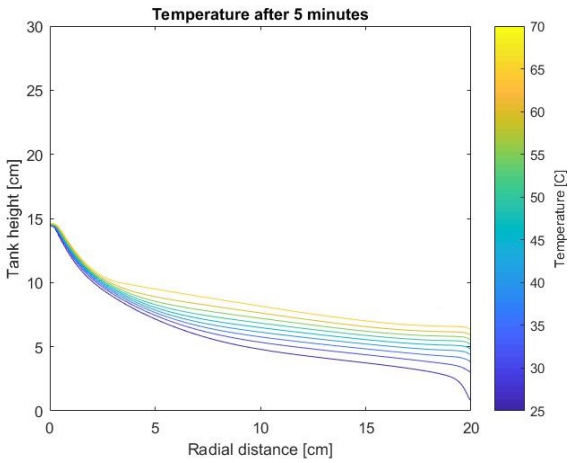
Temperature after 5 minutes
Tank height [cm]
Radial distance [cm]
Temperature [C]

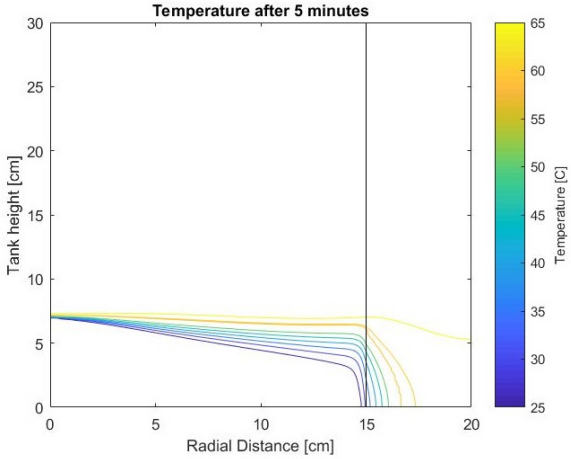
Temperature after 5 minutes
Tank height [cm]
Radial Distance [cm]
Temperature [C]

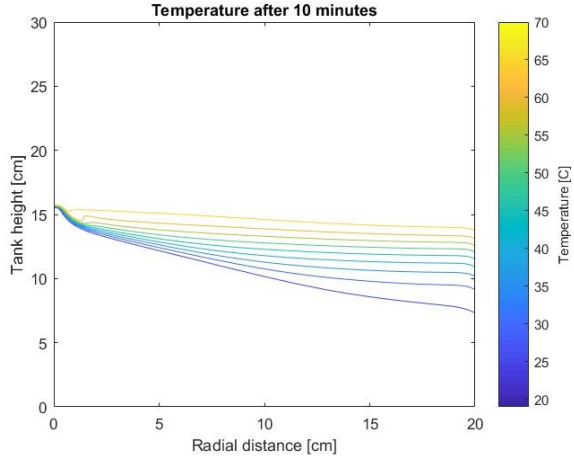
Temperature after 10 minutes
Tank height [cm]
Radial distance [cm]
Temperature [C]

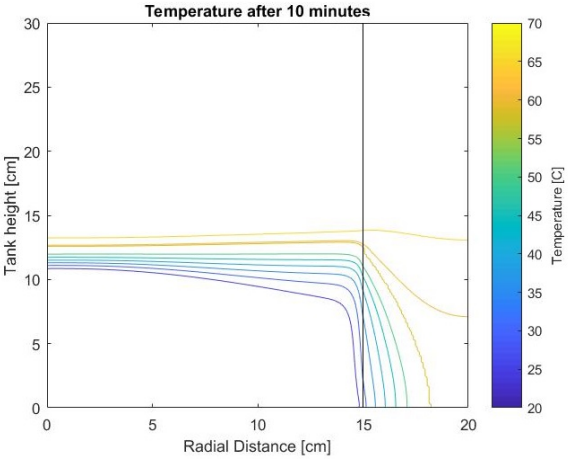
Temperature after 10 minutes
Tank height [cm]
Radial Distance [cm]
Temperature [C]

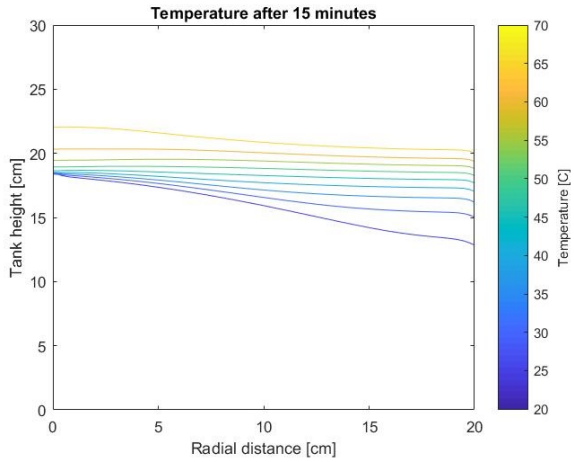
Temperature after 15 minutes
Tank height [cm]
Radial distance [cm]
Temperature [C]

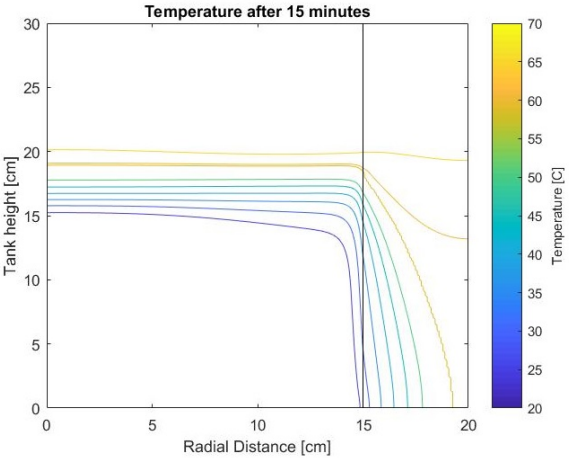
Temperature after 15 minutes
Tank height [cm]
Radial Distance [cm]
Temperature [C]

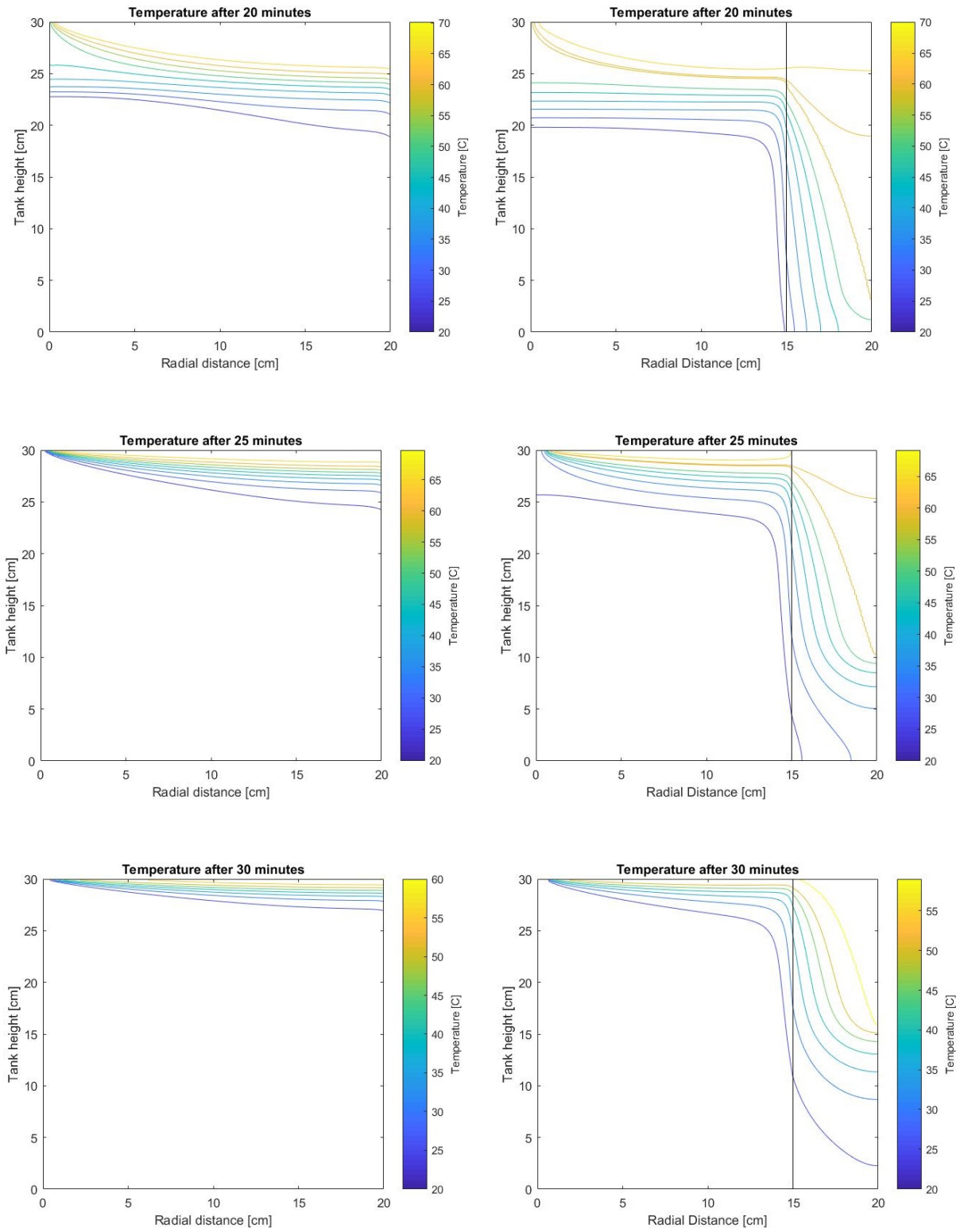

Figure 10: *Temperature contours of the conventional hot water tank (left) and the PCM-enhanced hot water tank (right) every 5 minutes in the simulation.*

The stream function contours have been generated in the middle of the simulation (after 15 minutes). Comparable stream function contours were obtained at other time instants. The results are shown in figure 11. The conventional hot water tank has a Richardson number of 0.35 which is lower than the Richardson number of the PCM-enhanced hot water tank: 1.33. Thus for the conventional hot water tank, the cold jet will penetrate deeper into the hot fluid because the momentum of the inlet jet is much bigger than the momentum of the buoyancy. This can be seen from the stream function contours and the temperature contours after 5 and 10 minutes. At 15 minutes, the moving thermocline is above the jet penetration height and this effect is less visible.

A higher Richardson number also increases the performance of the hot water tank: the (axial) temperature gradient of the thermocline will have a smaller thickness at high Richardson numbers. A steeper outlet temperature profile is therefore expected for the PCM-enhanced hot water tank. The higher Richardson number originates from the different flow rates for both tanks and is independent of the PCM that is present outside the tank. After 10 and 15 minutes the axial thickness of the temperature gradient of the PCM-enhanced hot water tank is clearly smaller than for the conventional hot water tank. At later times, the PCM at the lower regions releases its sensible and latent heat to the water which results in a thicker thermocline.

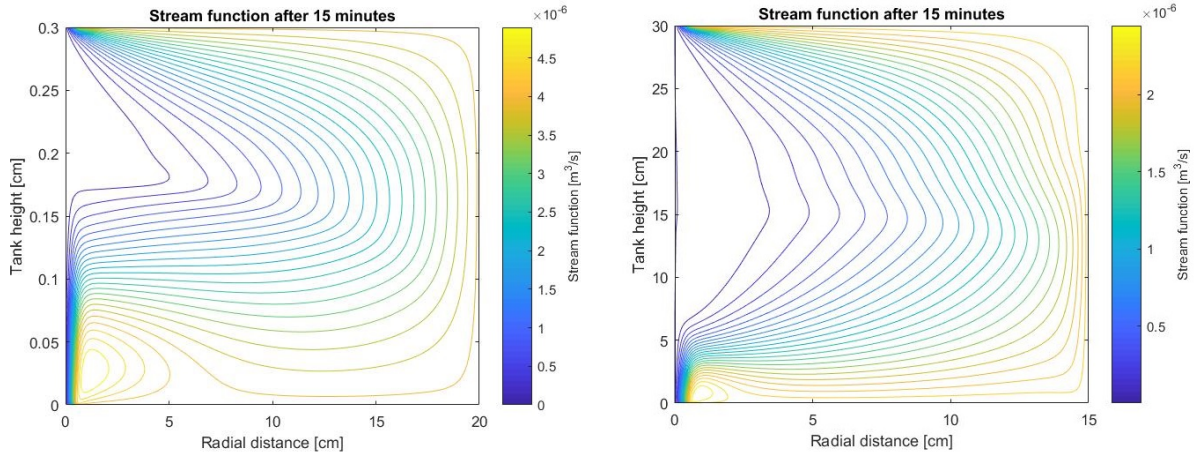

Figure 11: *Stream function contours for the conventional hot water tank (left) and the PCM-enhanced hot water tank (right) after 15 minutes. Comparable results were found at other time instants.*

After 30 minutes, the outlet temperature for both systems is 20 °C, indicating the end of the discharge cycle. The temperature of the fluid near the top wall is still warmer for both systems, but the outlet temperature was defined as the temperature at $(h, \Delta r)$. At this time, it can be seen that part of the PCM is still in its liquid state and its latent heat has not been provided to the water. Based on these simulations, approximately 2.3 kg of PCM is still liquid, meaning that 473 kJ or (0.47 MJ) has not been provided to the water. Still 16.9% of the PCM is liquid. The response time of the PCM is too slow while the flow rate already has been lowered to match the flow rate of the conventional hot water tank. At flow rates of 3.0 L/min, which are common for hot water tanks this size, the water is discharged at an even faster rate for the PCM-enhanced hot water tank. Resulting in even less PCM that would be able to release its latent heat to the water.

The outlet temperatures for both tanks have been presented as a function of time in figure 12. It can be seen that the outlet temperature of the PCM-enhanced hot water tank remains at a higher temperature for a longer period of time due to the presence of the PCM. However, in reality, the volumetric flow rate of cold water would be higher for the PCM-enhanced hot water tank which would decrease this effect. Furthermore, not all available energy was released during the discharge cycle. The theoretical performance of the PCM-enhanced hot water tank is therefore worse than for the conventional hot water tank.

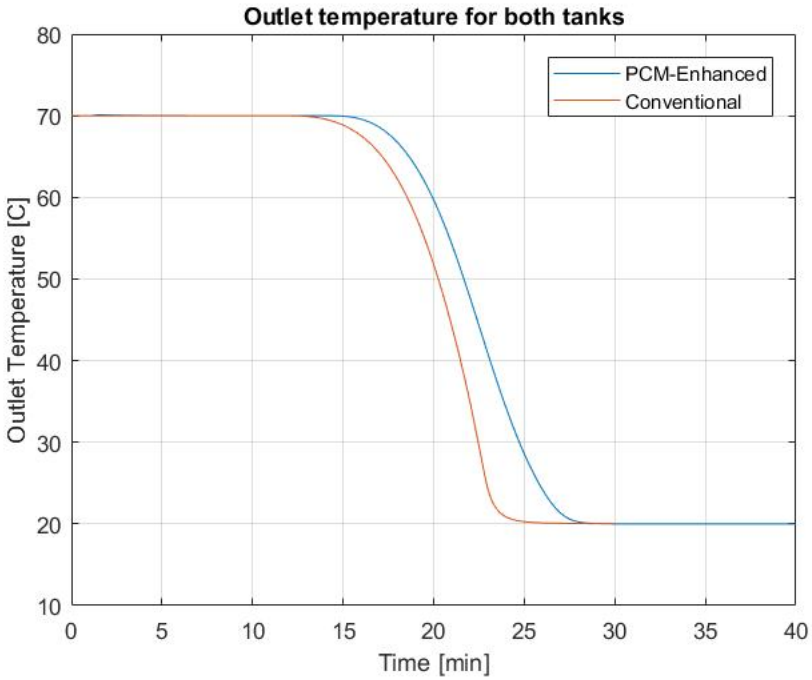

Figure 12: *Outlet temperature for both tanks.*

7 Conclusion

The aim of this research paper was to investigate the applicability of a domestic hot water tank with an increased heat capacity. To increase the heat capacity of the tank, part of the volume from the conventional hot water tank was substituted by a PCM. Three aspects were investigated regarding the performance of such a tank: the most suitable PCM type, the weak spots during the charging period of the tank and the response time of the PCM during the discharging of the tank. Comparisons were made with the conventional hot water tank having the same total volume. The following conclusions were drawn:

- The most suitable type of PCM for domestic applications turned out to be a paraffin based PCM: RT 60 Rubitherm. Paraffin based PCMs are stable and keep their thermal properties for long periods of time without degrading. RT 60 Rubitherm has a high latent heat (214 kJ/kg) and a suitable phase change temperature for the application of domestic hot water tanks (58 °C - 60 °C). The conductivity of RT 60 Rubitherm is low (0.2 W/(mK)) and therefore a method had to be applied to enhance the thermal conductivity and in return, the heat transfer rate. In this paper dispersion of a high density material (alumina) has been applied due to its easy implementation in the simulations, but the particle settling and Brownian motion had been ignored. Also the relatively high volume change has been ignored. Adding 500 grams of alumina increased the conductivity from 0.2 W/(mK) to 1.0 W/(mK).

- Although the simulations didn't reach the asymptotic range of convergence, some general conclusions could be drawn. Melting a Rubitherm layer with 5.0 cm thickness takes up a very long time (» 9 hours) while using this particular thickness does not theoretically increase the heat capacity of the tank. Instead, using this thickness keeps the heat capacity constant. Slow heat transfer rates are present when applying a 11.0 °C temperature difference between the maximum allowable tank temperature and the phase change temperature of the PCM. Convection during the solid-liquid phase change has been ignored.

- Since stratification will occur during charging, the PCM will melt at the slowest rate in the outer lower corners of the annular space, based on diffusive heat transfer through the PCM only.

- Although results indicate better performance for the discharge cycle when using PCM, a reduced flow rate was used and more PCM would be required to increase the capacity.

- Even at a reduced flow rate (1.69 L/min instead of 3.00 L/min), not all PCM was able to solidify during the discharge cycle: 16.9% of the PCM was still liquid at the end of the cycle. This means that 2.3 kg has not been melted, so 473 kJ of latent heat is not released to the water. This also indicates that the response time of the PCM is too low.

From all those bullet points, a final conclusion can be drawn regarding the applicability of a PCM-enhanced hot water tank to increase the heat capacity.

Despite the fact that the charging cycle did not converge properly, it was shown that melting 5.0 cm of RT 60 Rubitherm is a very slow process. Especially at the outer lower corners, where PCM had not even melted after 9 hours of charging.

During the discharge cycle, the response time of the PCM to release its latent heat to the water is too slow, even at smaller flow rates.

Finally, even more PCM is required to theoretically increase the heat capacity of the hot water tank instead of keeping it constant as in this paper. In combination with the fact that the settling of high density particles and volume changes have been neglected in this paper, creating even more problems and complexity in reality, such a system is not applicable as a domestic hot water tank. However, some suggestions are made in the next section which may increase the tank performance of any future models (or experiments).

8 Recommendations and Future Work

As was concluded in this report, using a PCM thickness of 5.0 cm was not enough to increase the capacity of the tank. To increase the capacity of the hot water tank enhanced with PCM, more PCM or a PCM with a higher latent heat should be used. When more PCM would be added, the heat transfer rate between water and PCM should be increased. To increase the heat transfer rate between water and PCM, several future options are provided within this section.

First of all, the heater could be placed near the wall, which separates the water from the PCM instead of placing it at the center of the tank. This may increase the temperature of the copper walls and as a result, the overall heat transfer rate during the charging cycle.

Secondly, convective heat transfer through the PCM could be taken into account since this may contribute to an increase in heat transfer rate during the charging cycle.

Finally, placing fins (especially at the lower parts of the tank) may help contribute to an increase in heat transfer rates for both the charging as well as the discharging cycle.

When future work will be modeled, it is recommended to use different discretization methods for the convective terms. The CUPID, SUCCA and SUPER schemes are recommended. When future work will be an experimental study, it is recommended to also take into account the behaviour of the nanoparticles (Brownian motion, settling), to investigate to what extent the performance of the tank is influenced.

9 References

[1] Itard, L. (2012). Energy in the built environment. In *Sustainable Urban Environments* (pp. 113-175). Springer, Dordrecht.

[2] Belz, K., Kuznik, F., Werner, K. F., Schmidt, T., & Ruck, W. K. L. (2015). Thermal energy storage systems for heating and hot water in residential buildings. In *Advances in Thermal Energy Storage Systems* (pp. 441-465). Woodhead Publishing.

[3] Sarbu, I., & Dorca, A. (2019). Review on heat transfer analysis in thermal energy storage using latent heat storage systems and phase change materials. *International Journal of Energy Research, 43*(1), 29-64.

[4] Bruno, F., Belusko, M., Liu, M., & Tay, N. H. S. (2015). Using solid-liquid phase change materials (PCMs) in thermal energy storage systems. In *Advances in thermal energy storage systems* (pp. 201-246). Woodhead Publishing.

[5] Gaeini, M. (2017). Thermochemical seasonal heat storage for the built environment: a multi-scale investigation.

[6] Aydin, D., Casey, S. P., & Riffat, S. (2015). The latest advancements on thermochemical heat storage systems. *Renewable and Sustainable Energy Reviews, 41*, 356-367.

[7] Sharma, A., Tyagi, V. V., Chen, C. R., & Buddhi, D. (2009). Review on thermal energy storage with phase change materials and applications. *Renewable and Sustainable energy reviews, 13*(2), 318-345.

[8] Kenisarin, M., & Mahkamov, K. (2007). Solar energy storage using phase change materials. *Renewable and sustainable energy reviews, 11*(9), 1913-1965.

[9] Jegadheeswaran, S., Pohekar, S. D., & Kousksou, T. (2011). Performance enhancement of solar latent heat thermal storage system with particle dispersion—an exergy approach. *Clean–Soil, Air, Water, 39*(10), 964-971.

[10] Ho, C. J., & Gao, J. Y. (2009). Preparation and thermophysical properties of nanoparticle-in-paraffin emulsion as phase change material. *International Communications in Heat and Mass Transfer, 36*(5), 467-470.

[11] Mettawee, E. B. S., & Assassa, G. M. (2007). Thermal conductivity enhancement in a latent heat storage system. *Solar Energy, 81*(7), 839-845.

[12] Frusteri, F., Leonardi, V., Vasta, S., & Restuccia, G. (2005). Thermal conductivity measurement of a PCM based storage system containing carbon fibers. *Applied thermal engineering, 25*(11-12), 1623-1633.

[13] Nakaso, K., Teshima, H., Yoshimura, A., Nogami, S., Hamada, Y., & Fukai, J. (2008). Extension of heat transfer area using carbon fiber cloths in latent heat thermal energy storage tanks. *Chemical Engineering and Processing: Process Intensification, 47*(5), 879-885.

[14] Sarı, A., & Karaipekli, A. (2007). Thermal conductivity and latent heat thermal energy storage characteristics of paraffin/expanded graphite composite as phase change material. *Applied thermal engineering, 27*(8-9), 1271-1277.

[15] Lafdi, K., Mesalhy, O., & Shaikh, S. (2007). Experimental study on the influence of foam porosity and pore size on the melting of phase change materials. *Journal of Applied Physics, 102*(8), 083549.

[16] Zhou, D., & Zhao, C. Y. (2011). Experimental investigations on heat transfer in phase change materials (PCMs) embedded in porous materials. *Applied Thermal Engineering, 31*(5), 970-977.

[17] Shchukina, E. M., Graham, M., Zheng, Z., & Shchukin, D. G. (2018). Nanoencapsulation of phase change materials for advanced thermal energy storage systems. *Chemical Society Reviews, 47*(11), 4156-4175.

[18] Wang, Z., Zhang, H., Dou, B., Huang, H., Wu, W., & Wang, Z. (2017). Experimental and numerical research of thermal stratification with a novel inlet in a dynamic hot water storage tank. *Renewable Energy, 111*, 353-371.

[19] Unrau, C. (2017). *Numerical investigation of one-dimensional storage tank models and the development of analytical modelling techniques* (Doctoral dissertation).

[20] Kleinbach, E. M., Beckman, W. A., & Klein, S. A. (1993). Performance study of one-dimensional models for stratified thermal storage tanks. *Solar energy, 50*(2), 155-166.

[21] Zurigat, Y. H., Liche, P. R., & Ghajar, A. J. (1991). Influence of inlet geometry on mixing in thermocline thermal energy storage. *International Journal of Heat and Mass Transfer, 34*(1), 115-125.

[22] Nizami, D. J., Lightstone, M. F., Harrison, S. J., & Cruickshank, C. A. (2013). Negative buoyant plume model for solar domestic hot water tank systems incorporating a vertical inlet. *Solar energy, 87*, 53-63.

[23] Torrance, K. E. (1968). Comparison of Finite-Difference Computations. *Journal of Research of the National Bureau of Standards: Mathematical sciences. B, 72*, 281.

[24] Torrance, K. E., & Rockett, J. A. (1969). Numerical study of natural convection in an enclosure with localized heating from below—creeping flow to the onset of laminar instability. *Journal of Fluid Mechanics, 36*(1), 33-54.

[25] Hahne, E., & Chen, Y. (1998). Numerical study of flow and heat transfer characteristics in hot water stores. *Solar energy, 64*(1-3), 9-18.

[26] Cai, L., Stewart Jr, W. E., & Sohn, C. W. (1993). Turbulent buoyant flows into a two dimensional storage tank. *International journal of heat and mass transfer, 36*(17), 4247-4256.

[27] Tacke, K. H. (1985). Discretization of the explicit enthalpy method for planar phase change. *International journal for numerical methods in engineering, 21*(3), 543-554.

[28] Swan, L. G., & Ugursal, V. I. (2009). Modeling of end-use energy consumption in the residential sector: A review of modeling techniques. *Renewable and sustainable energy reviews, 13*(8), 1819-1835.

[29] Mostafa, M. H., Aleem, S. H. A., Ali, S. G., & Abdelaziz, A. Y. (2019). Energy-management solutions for microgrids. In *Distributed Energy Resources in Microgrids* (pp. 483-515). Academic Press.

[30] Pérez-Lombard, L., Ortiz, J., & Pout, C. (2008). A review on buildings energy consumption information. *Energy and buildings, 40*(3), 394-398.

[31] Roache, P. J. (1994). Perspective: a method for uniform reporting of grid refinement studies.

[32] Torrance, K., Davis, R., Eike, K., Gill, P., Gutman, D., Hsui, A.,& Zien, H. (1972). Cavity flows driven by buoyancy and shear. *Journal of Fluid Mechanics, 51*(2), 221-231.

[33] Karadimou, D. P., & Markatos, N. C. (2018). Study of the Numerical Diffusion in Computational Calculations. *Numerical Simulations in Engineering and Science*, 65.

[34] Durakovic, B., & Torlak, M. (2017). Simulation and experimental validation of phase change material and water used as heat storage medium in window applications. *J. of Mater. and Environ. Sci, 8*(5), 1837-1846.

[35] Kundu, P. K., Cohen, I. M., & Dowling, D. (2016). Fluid Mechanics 6th.

10 Appendix A: Numerical Results for Grid Dependency Tests for Charging Model

	Conventional Hot Water Tank					
	Coarse Grid (36x24)		Medium Grid (54x36)		Fine Grid (81x54)	
Simulation Time	Ψ_{max} [m^3/s]	Ω_{max} [Hz]	Ψ_{max} [m^3/s]	Ω_{max} [Hz]	Ψ_{max} [m^3/s]	Ω_{max} [Hz]
15 min.	$8.45 \cdot 10^{-5}$	15.61	$3.05 \cdot 10^{-5}$	19.91	$1.28 \cdot 10^{-5}$	28.70
30 min.	$6.02 \cdot 10^{-5}$	12.31	$1.99 \cdot 10^{-5}$	16.81	$1.09 \cdot 10^{-5}$	26.37
45 min.	$5.49 \cdot 10^{-5}$	9.66	$2.10 \cdot 10^{-5}$	14.57	$9.06 \cdot 10^{-6}$	18.19
60 min.	$5.19 \cdot 10^{-5}$	10.00	$2.00 \cdot 10^{-5}$	9.48	$1.04 \cdot 10^{-5}$	17.36
	PCM-Enhanced Hot Water Tank					
	Coarse Grid (36x24)		Medium Grid (54x36)		Fine Grid (81x54)	
Simulation Time	Ψ_{max} [m^3/s]	Ω_{max} [Hz]	Ψ_{max} [m^3/s]	Ω_{max} [Hz]	Ψ_{max} [m^3/s]	Ω_{max} [Hz]
15 min.	$5.45 \cdot 10^{-5}$	18.46	$2.16 \cdot 10^{-5}$	27.95	$8.85 \cdot 10^{-6}$	38.07
30 min.	$5.50 \cdot 10^{-5}$	15.88	$1.81 \cdot 10^{-5}$	23.71	$7.11 \cdot 10^{-6}$	32.11
45 min.	$4.14 \cdot 10^{-5}$	13.68	$1.51 \cdot 10^{-5}$	22.13	$6.41 \cdot 10^{-6}$	26.15
60 min.	$4.37 \cdot 10^{-5}$	14.66	$1.59 \cdot 10^{-5}$	17.81	$7.02 \cdot 10^{-6}$	22.33
90 min.	$3.52 \cdot 10^{-5}$	12.30	$1.26 \cdot 10^{-5}$	16.64	$5.19 \cdot 10^{-6}$	19.77
3 hrs.	$2.34 \cdot 10^{-5}$	9.10	$9.84 \cdot 10^{-6}$	12.88	$5.48 \cdot 10^{-6}$	20.59
5 hrs.	$2.54 \cdot 10^{-5}$	8.00	$1.38 \cdot 10^{-5}$	13.47	$4.66 \cdot 10^{-6}$	18.31
7 hrs.	$2.40 \cdot 10^{-5}$	11.03	$1.17 \cdot 10^{-5}$	16.30	$5.62 \cdot 10^{-6}$	18.51
9 hrs.	$1.92 \cdot 10^{-5}$	10.11	$9.60 \cdot 10^{-6}$	11.42	$6.38 \cdot 10^{-6}$	14.77

Table 8: *Maximum values for stream function and vorticity for different mesh types both for the conventional and the PCM-enhanced hot water tank during the charging cycle. Also, the maximum values of the vorticity are shown.*

	Conventional Hot Water Tank				
	Stream Function Ψ				
Simulation Time	p	GCI_{12} [%]	GCI_{23} [%]	ARC	True Value [m^3/s]/[Hz]
15 min.	2.75	84.3%	108%	0.42	N.A.
30 min.	3.70	29.7%	72.8%	0.55	N.A.
45 min.	2.57	89.6%	110%	0.43	N.A.
60 min.	2.96	49.7%	85.8%	0.52	N.A.

	PCM-Enhanced Hot Water Tank				
	Stream Function Ψ / Vorticity Ω [Hz]				
Simulation Time	p	GCI_{12} [%]	GCI_{23} [%]	ARC	True Value [m^3/s]/[Hz]
15 min.	2.35	113%	120%	0.41	N.A.
30 min.	2.99	82.0%	108%	0.39	N.A.
45 min.	2.73	83.6%	107%	0.42	N.A.
60 min.	2.81	74.2%	103%	0.44	N.A.
90 min.	2.75	87.1%	109%	0.41	N.A.
3 hrs.	2.80	47.1%	81.6%	0.56	N.A.
5 hrs.	0.59	911%	390%	0.34	N.A.
7 hrs.	1.74	132%	128%	0.48	N.A.
9 hrs.	2.69	31.8%	63.1%	0.66	N.A.

Table 9: *Results of the spatial grid dependency tests for the charging model. Both the conventional and the PCM-enhanced hot water tank are shown. The Richard exptrapolated values are not applicable (N.A.), since results are too far from the asymptotic range of convergence.*

11 Appendix B: Figures of Charging Model

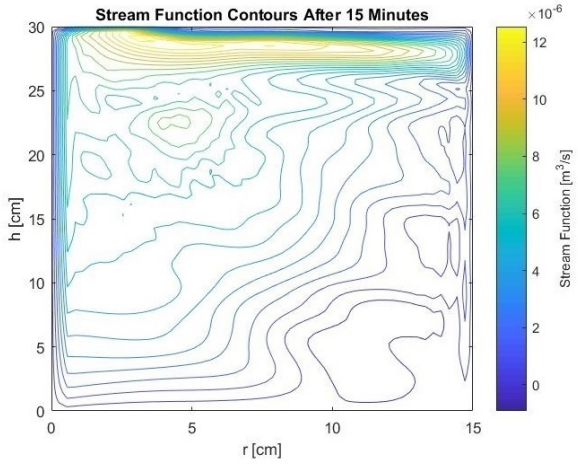

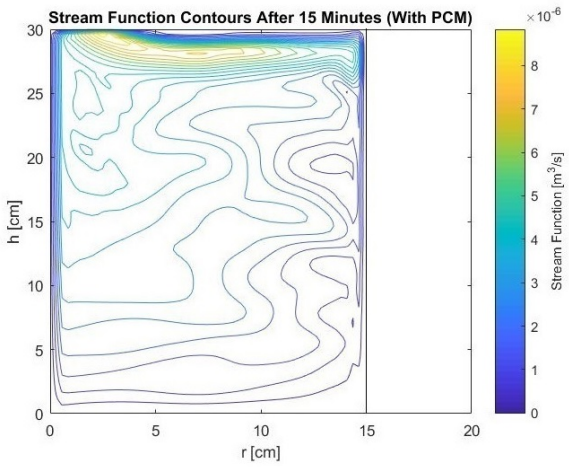

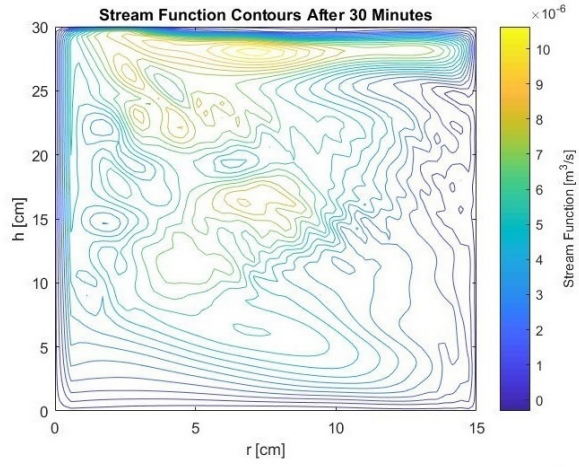

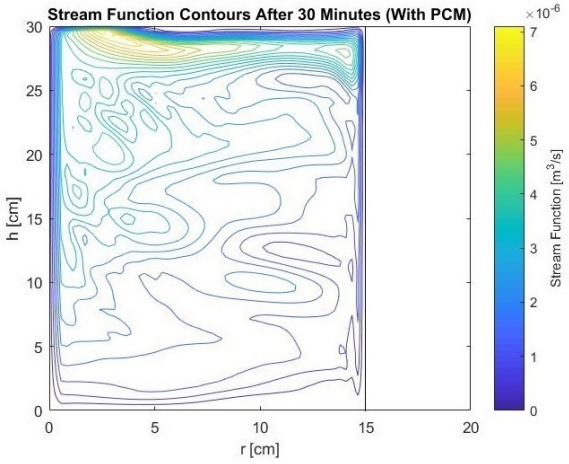

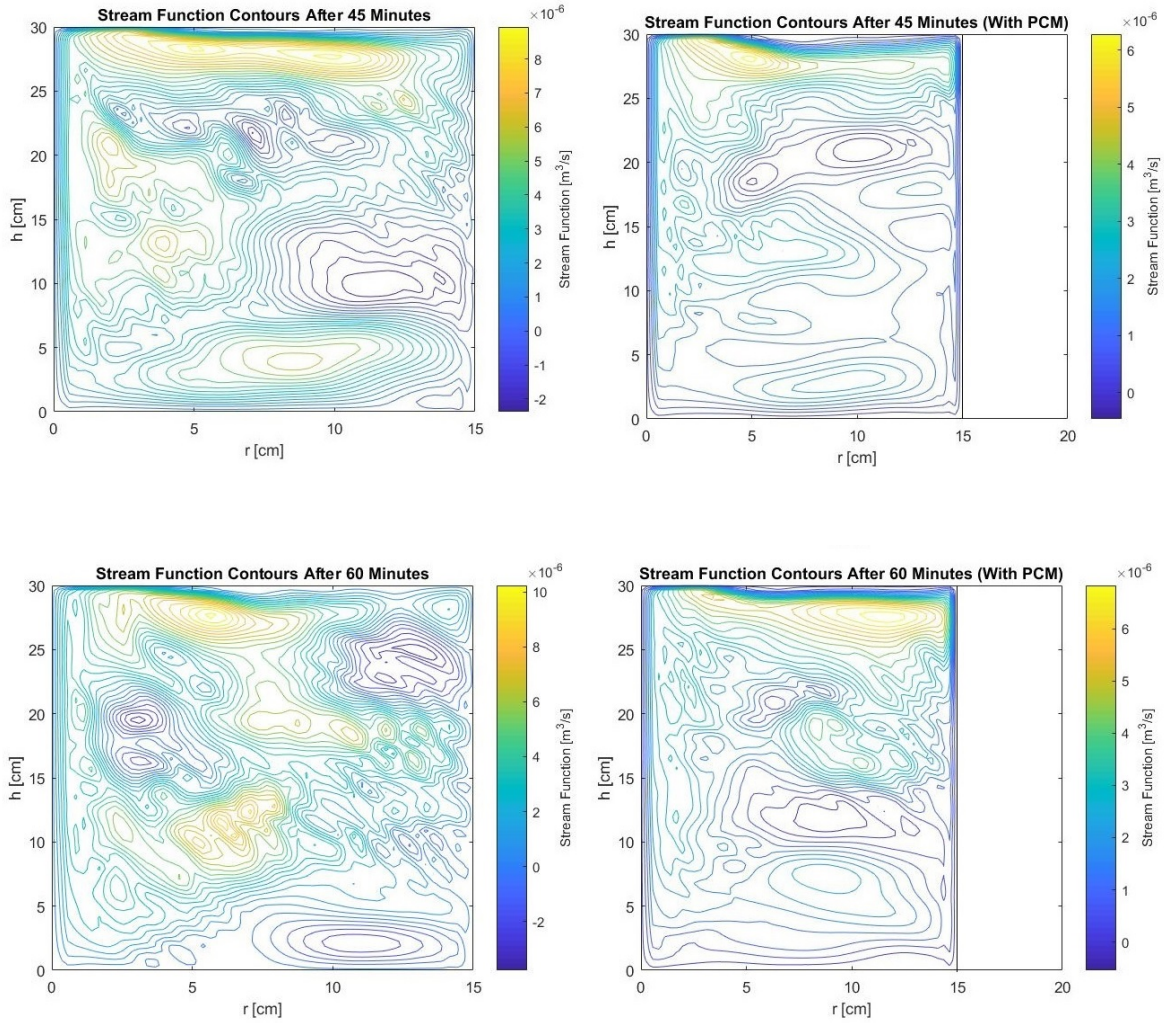

Figure 13: *Stream functions for the conventional hot water tank (left) and the PCM-enhanced hot water tank (right). Notice that the region 15-20 cm of the PCM-enhanced hot water tank only consists of PCM and thus the stream functions are absent.*

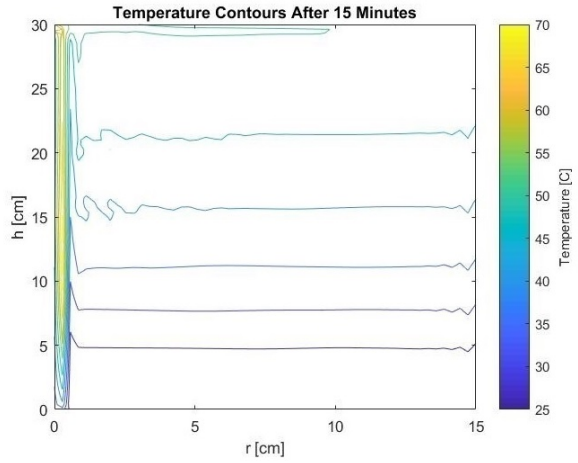
Temperature Contours After 15 Minutes
h [cm]
r [cm]
Temperature [C]

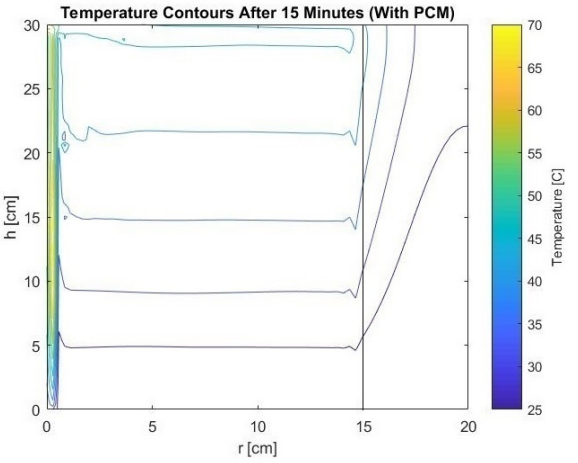
Temperature Contours After 15 Minutes (With PCM)
h [cm]
r [cm]
Temperature [C]

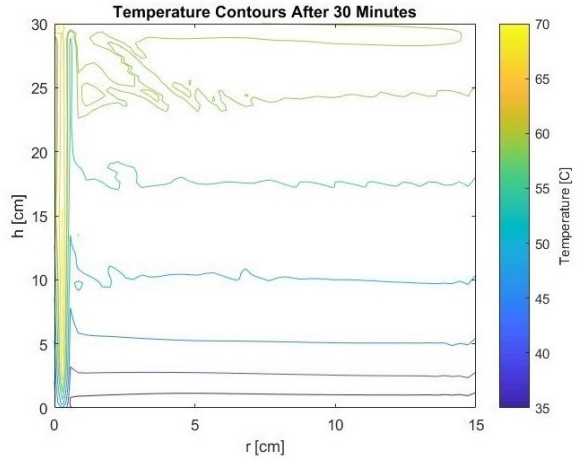
Temperature Contours After 30 Minutes
h [cm]
r [cm]
Temperature [C]

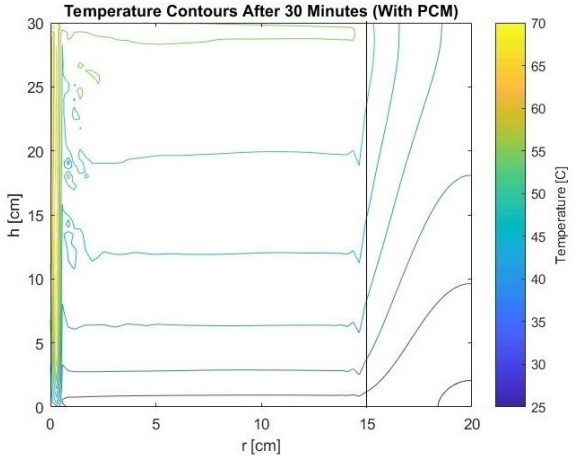
Temperature Contours After 30 Minutes (With PCM)
h [cm]
r [cm]
Temperature [C]

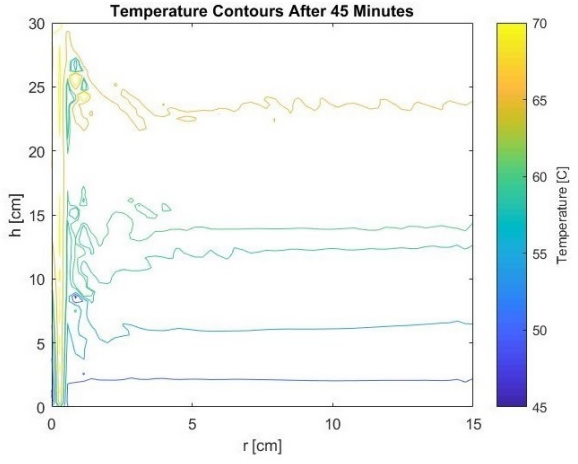
Temperature Contours After 45 Minutes
h [cm]
r [cm]
Temperature [C]

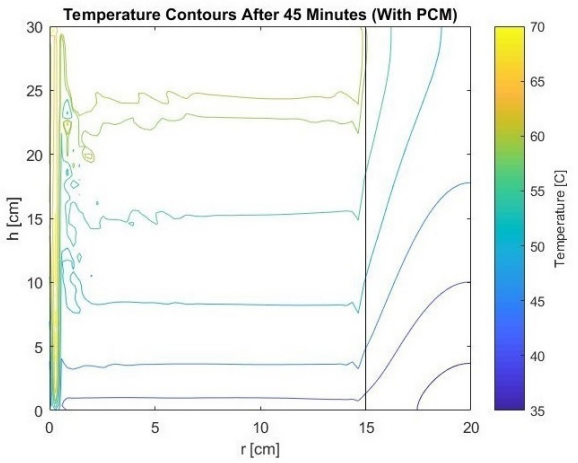
Temperature Contours After 45 Minutes (With PCM)
h [cm]
r [cm]
Temperature [C]

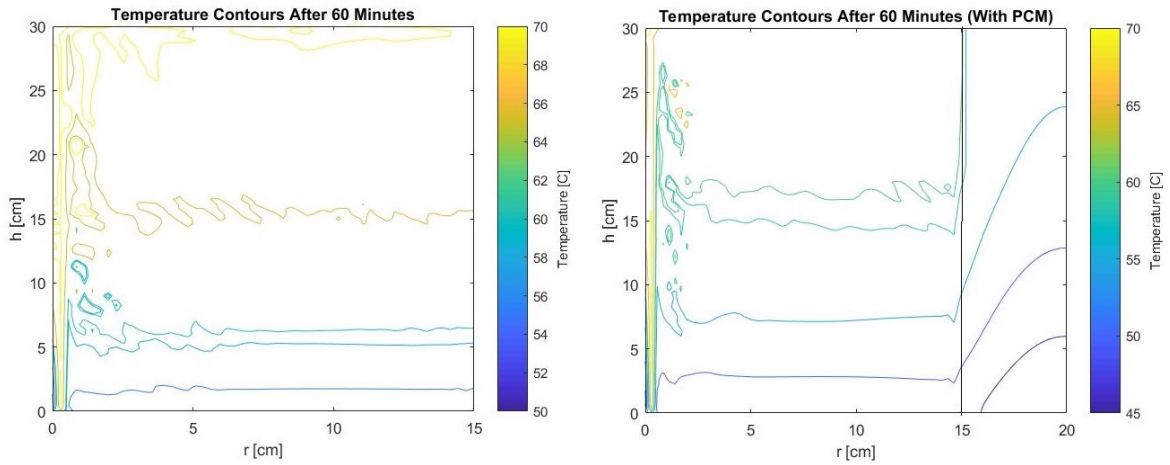

Figure 14: *Temperature contours for the conventional hot water tank (left) and the PCM-enhanced hot water tank (right). After 60 minutes, the PCM starts to melt and an additional contour has been added of 59 - 60 °C to indicate the melting profile.*

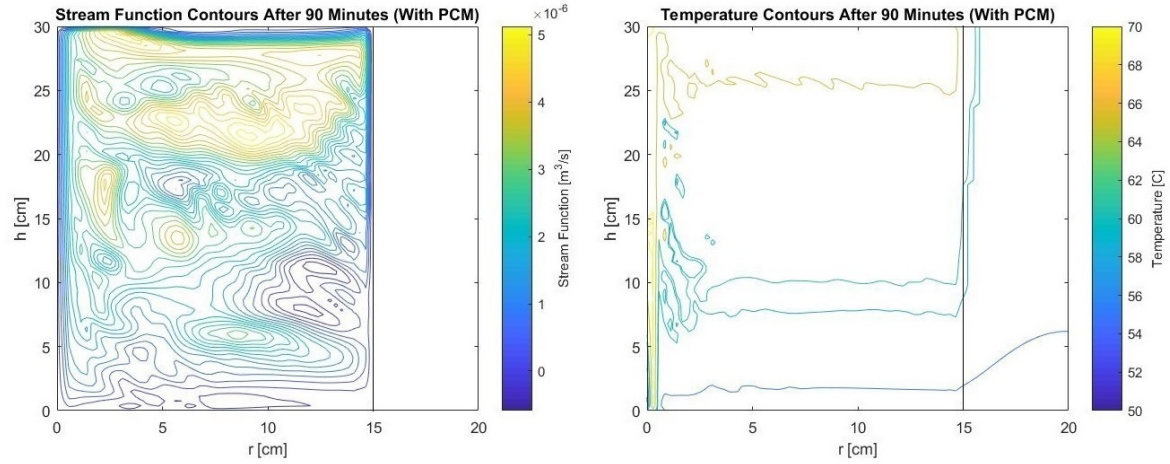

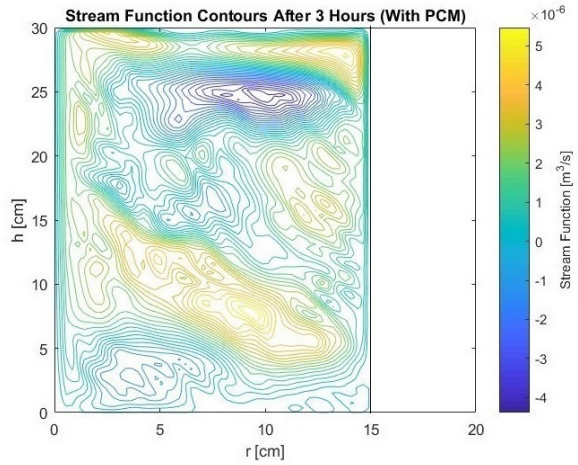
Stream Function Contours After 3 Hours (With PCM)
h [cm]
r [cm]
Stream Function [m^3/s]
×10^-6

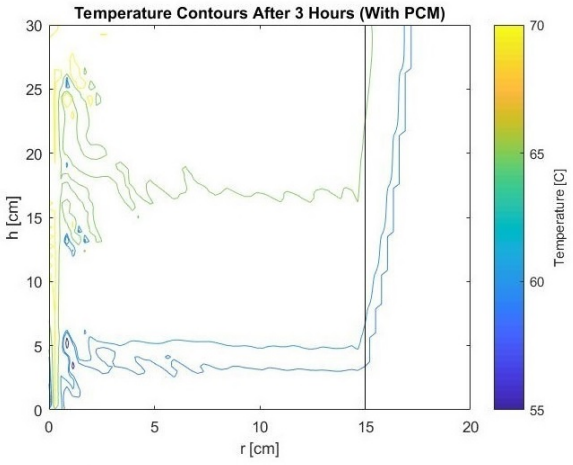
Temperature Contours After 3 Hours (With PCM)
h [cm]
r [cm]
Temperature [C]

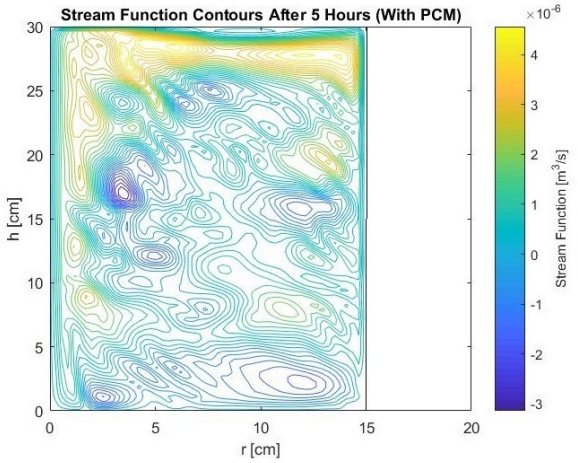
Stream Function Contours After 5 Hours (With PCM)
h [cm]
r [cm]
Stream Function [m^3/s]
×10^-6

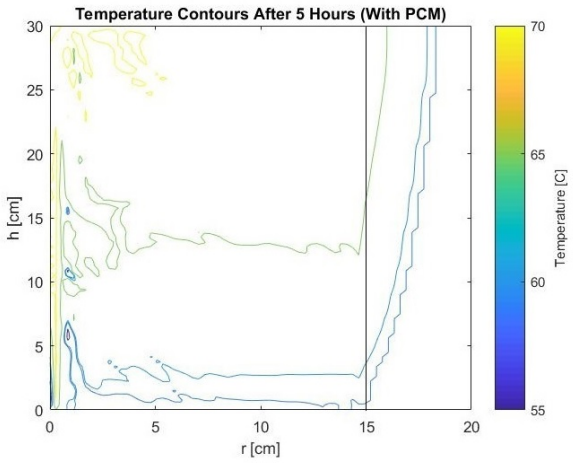
Temperature Contours After 5 Hours (With PCM)
h [cm]
r [cm]
Temperature [C]

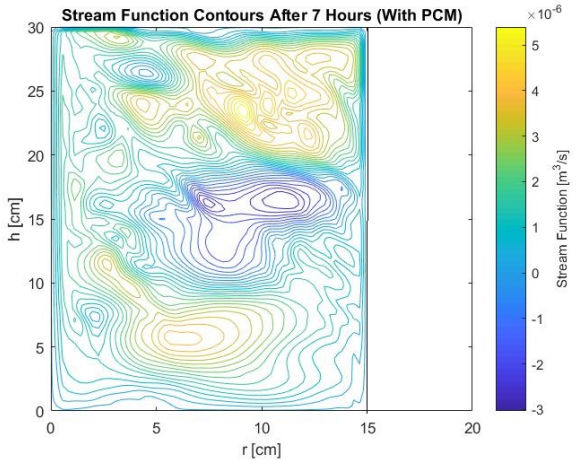
Stream Function Contours After 7 Hours (With PCM)
h [cm]
r [cm]
Stream Function [m^3/s]
×10^-6

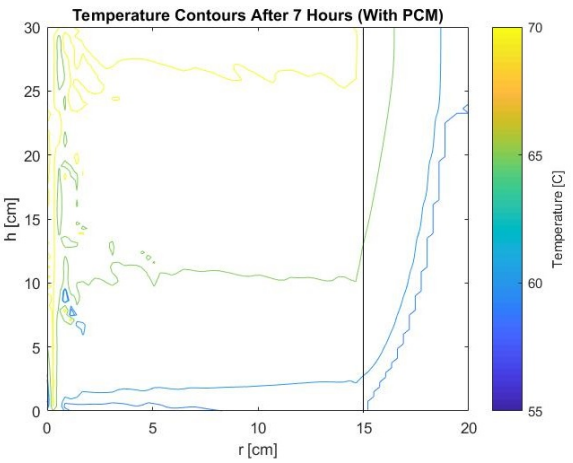
Temperature Contours After 7 Hours (With PCM)
h [cm]
r [cm]
Temperature [C]

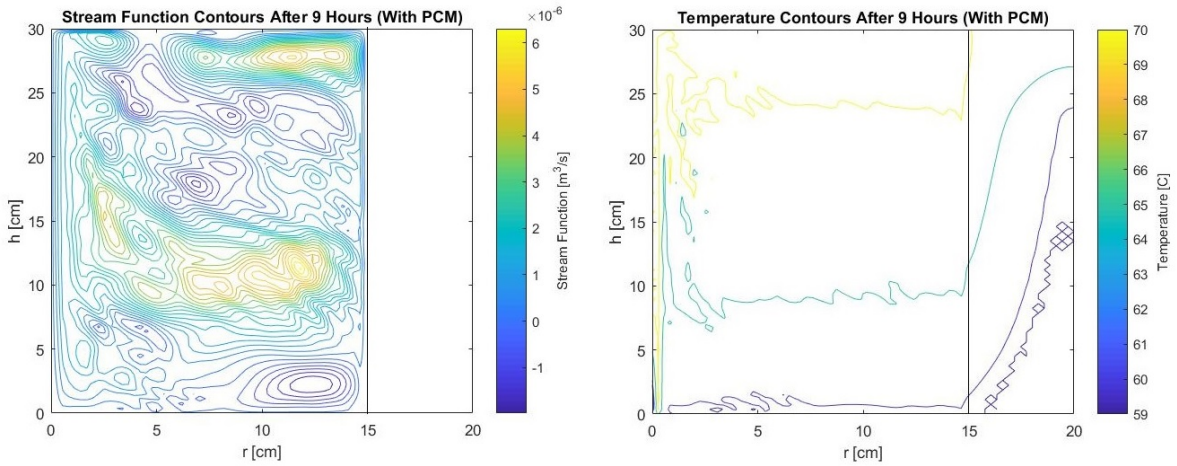

Figure 15: *Stream functions and temperature contours for the PCM-enhanced hot water tank after long periods of time. The melting is clearly visible.*

12 Appendix C: Derivation of the buoyancy source terms

In this section the derivation will be shown for the buoyancy source terms for both models in dimensionless form. To arrive at the vorticity equation, the curl of the momentum equation should be evaluated, since $\Omega = \vec{\Delta} \times \vec{u}$. When applying the curl operator to the momentum equation the vorticity equation is obtained [35] (pp. 212-213):

$$\frac{D\vec{\Omega}}{Dt} = \vec{\Omega} \cdot \vec{\nabla}\vec{u} + \nu\vec{\nabla}^2\vec{\Omega} + \left[\frac{1}{\rho^2}\vec{\nabla}\rho \times \vec{\nabla}p\right] \tag{92}$$

The buoyancy source term originates from the term in between brackets in equation 92. This term is called baroclinity and represents generation of vorticity due to the density differences [35]. This term can be rewritten as:

$$\frac{1}{\rho^2}\vec{\nabla}\rho \times \vec{\nabla}p = \frac{1}{\rho^2}\left[\frac{\partial\rho}{\partial r}\frac{\partial p}{\partial z} - \frac{\partial p}{\partial r}\frac{\partial\rho}{\partial z}\right] \tag{93}$$

Using the hydrostatic equations,

$$\frac{\partial p}{\partial r} = 0 \quad \frac{\partial p}{\partial z} = -\rho g \tag{94}$$

equation 93 can be rewritten as:

$$\frac{1}{\rho^2}\vec{\nabla}\rho \times \vec{\nabla}p = \frac{1}{\rho^2}\left[-\rho g\frac{\partial\rho}{\partial r}\right] = -g\left(\frac{1}{\rho}\frac{\partial\rho}{\partial r}\right) \tag{95}$$

If it is assumed that the density varies linearly, the following relation can be used [35] (pp. 153-155):

$$\rho = \rho_0[1 - \beta(T - T_0)] \tag{96}$$

The thermal expansion coefficient is denoted by β. The term ρ_0 is a reference pressure. In terms of temperature, this linear relation can be rewritten as:

$$(T - T_0) = \frac{1}{\beta}\left(\frac{\rho_0 - \rho}{\rho_0}\right) \approx \frac{1}{\beta}\frac{\partial\rho}{\rho_0} \tag{97}$$

The change in density is required for equation 95 to find an expression in terms of temperature. Thus:

$$\partial\rho = \rho_0\beta\partial T \tag{98}$$

This expression is substituted into equation 95. Note that ρ has been replaced by ρ_0 in equation 95, since the pressure is the reference pressure. Since ρ_0, β and T_0 are constants, the following expression is found:

$$-g\left(\frac{1}{\rho_0}\frac{\partial\rho}{\partial r}\right) = -g\left(\frac{1}{\rho_0}\rho_0\beta\frac{\partial T}{\partial r}\right) \tag{99}$$

The final expression for the buoyancy terms is the following:

$$\frac{1}{\rho^2}\vec{\nabla}\rho \times \vec{\nabla}p = -g\beta\frac{\partial T}{\partial r} \tag{100}$$

If this term is converted to a non-dimensional form, using the dimensionless parameters mentioned in the paper, it takes the following form (for both models):

$$-g\beta\frac{\partial T}{\partial r} \rightarrow -\frac{g\beta(T_h - T_0)}{h}\frac{\partial\theta}{\partial R} \tag{101}$$

Where θ and R are dimensionless temperature and radial distance respectively. For the charging model this term is multiplied by h^4/α^2, which is a constant coming from non-dimensionalizing the vorticity equation. The buoyancy source term then becomes:

$$-\frac{g\beta(T_h - T_0)h^4}{\alpha^2 h}\frac{\partial\theta}{\partial R} = -\frac{g\beta(T_h - T_0)h^3}{\alpha^2}\frac{\partial\theta}{\partial R} = -\mathrm{GrPr}^2\frac{\partial\theta}{\partial R} \tag{102}$$

Which is used in this report.

For the discharging cycle, the term from 100 is multiplied by h^2/u_{jet}^2, which is again a constant from non-dimensionalizing the governing equation. It is then found that:

$$-g\beta\frac{\partial T}{\partial r} \rightarrow -\frac{g\beta(T_h - T_0)}{h}\cdot\frac{h^2}{u_{\mathrm{jet}}^2}\frac{\partial\theta}{\partial R} = -\mathrm{Ri}\frac{\partial\theta}{\partial R} \tag{103}$$

Note that in the model for discharging the tank a modified vorticity (Ω') has been used in such a way that $\Omega = \Omega' R$. This results in multiplying constant R with every term that contains the vorticity. For the vorticity equation, all terms contain the vorticity except for the buoyancy term. That means that every R cancels except for the buoyancy term where a $1/R$ will appear. So finally it is indeed found that in the nondimensional equation for the vorticity, the buoyancy source term is given by:

$$-\frac{\mathrm{Ri}}{R}\frac{\partial\theta}{\partial R} \tag{104}$$